CHARACTERIZATION AND MITIGATION OF RESISTIVE LOSSES IN A LARGE AREA LASER POWER CONVERTER

THESIS

Eli A. Garduño, Second Lieutenant, USAF

AFIT-ENP-14-M-09

DEPARTMENT OF THE AIR FORCE
AIR UNIVERSITY

AIR FORCE INSTITUTE OF TECHNOLOGY

Wright-Patterson Air Force Base, Ohio

AFIT-ENP-14-M-09

CHARACTERIZATION AND MITIGATION OF RESISTIVE LOSSES IN A LARGE AREA LASER POWER CONVERTER

THESIS

Presented to the Faculty

Department of Engineering Physics

Graduate School of Engineering and Management

Air Force Institute of Technology

Air University

Air Education and Training Command

in Partial Fulfillment of the Requirements for the

Degree of Master of Science in Applied Physics

Eli A. Garduño, BS

Second Lieutenant, USAF

March 2014

AFIT-ENP-14-M-09

CHARACTERIZATION AND MITIGATION OF RESISTIVE LOSSES IN A LARGE AREA LASER POWER CONVERTER

Eli A. Garduño, BS
Second Lieutenant, USAF

Approved:

//signed//	13 March 2014
Maj Timothy W. Zens, PhD (Chairman)	Date
//signed//	17 March 2014
Glen Perram, PhD (Member)	Date
//signed//	13 March 2014
David Weyburne, PhD (Member)	Date

AFIT-ENP-14-M-09

Abstract

GaAs Laser Power Converters (LPC) were simulated in 2D and 3D under 10 W/cm^2 illumination of 810 nm light using Synopsys Sentaurus software revealing significant dependence of efficiency on grid metal finger spacings, S, and finger dimensions. Efficiency results were comparable to an experimental efficiency of 53.4% cited in the literature for an LPC under 43 W/cm^2 of 810 nm laser light. 2D devices were simulated with S of $20 - 1000$ μm revealing an efficiency drop, $\Delta\eta$, with increasing spacings. The efficiency drop was reduced from $\Delta\eta$ of 39.43% at $S = 740$ μm to $\Delta\eta$ of 14.38% at $S = 1000$ μm when modifying the window layer to include a highly doped lateral conduction layer (LCL). In the 3D simulations, resistive losses in the grid metal fingers were reduced by thickening the grid metal from 3 μm $\times$ 0.5 μm with an efficiency of 26% at an effective length of 0.5 cm up to 10 μm $\times$ 5 μm, achieving an efficiency of 44.89% at an effective finger length of 1 cm. An LCL and thicker fingers are shown to be critical for designing large area LPCs to convert laser light to electrical power for devices such as small RPAs and tactical sensors.

To my roommates

Acknowledgements

First, I would like to thank Dr. Vangala and Dr. Reyner for their contributions to this work. I would also like to thank Dr. Weyburne for making me a part of his team and guiding my efforts while allowing me the independence to grow as a researcher. Finally, I would like to express my sincere gratitude to my advisor, Maj Zens, for his investment in my development as both a scientist and an officer. I could not have asked for a better role model.

Eli A. Garduño

Table of Contents

Page

List of Figures

List of Tables

List of Symbols

Symbol		Page
R_s	total series resistance	17
I_{on}	reverse bias saturation current	17
I_{sc}	short-circuit current	20
V_{oc}	open-circuit voltage	20
R_G	front grid metal resistance	23
R_C	cap layer resistance	23
R_B	base resistance	23
R_{BSF}	back surface field resistance	23
R_{Bu}	buffer resistance	23
R_L	combined window and emitter resistance	23
R_E	emitter resistance	23
R_W	window resistance	23
S	finger spacing	24
L_f	finger length	24
W_f	finger width	24
W_b	bus width	24
ρ_e	sheet resistivity of window/emitter layer	24
J	extracted current density	25
ρ_f	bulk grid metal resistivity	26
L_s	shadowing loss	27
H_f	finger height	27
θ_i	incidence angle of illumination	27
ρ_{sc}	specific contant resistivity	28
w	transmission line width on TLM pads	29

List of Abbreviations

Abbreviation		Page
RPA	Remotely Piloted Aircraft	1
NASA	National Aeronautics and Space Administration	1
PV	Photovoltaic	1
LPC	Laser Power Converter	1
NIR	Near-Infrared	5
InGaAs	Indium Gallium Arsenide	5
InP	Indium Phosphide	5
TPV	Thermophotovoltaics	5
AFRL	Air Force Research Laboratory	6
MBE	Molecular Beam Epitaxy	6
TCAD	Technology Computer Aided Design	8
IV	current-voltage	17
SRH	Shockley Reed Hall	17
BSF	Back Surface Field	20
FF	Fill Factor	21
QE	Quantum Efficiency	21
EQE	External Quantum Efficiency	21
IQE	Internal Quantum Efficiency	21
TLM	Transmission Line Method	29
MOCVD	Metalorganic Chemical Vapor Deposition	29
MBE	Molecular Beam Epitaxy	29
BCSC	Buried Contact Solar Cell	30

Abbreviation		Page
VMJ	Vertical Multi-Junction	32
LCL	Lateral Conduction Layer	34
CPVs	Concentrator Photovoltaics	36
HMDS	Hexamethyldisilazane	43
TMM	Transfer Matrix Method	57
FLPC	Fraunhofer Institute based LPC	64
OLPC	Original Laser Power Converter	67
GRF	Gold Resistivity Factor	77

CHARACTERIZATION AND MITIGATION OF RESISTIVE LOSSES IN A LARGE AREA LASER POWER CONVERTER

I. Introduction

1.1 Motivation

Harnessing the power of the sun through solar cell technology has allowed for the sustained operation of a number of civilian and military technologies. There are, however, limitations that preclude solar technology as a viable source of energy for large scale and mission critical equipment such as Remotely Piloted Aircraft (RPA) [1]. First, the sun is not available during the night and can be blocked by clouds during part or all of the day. Second, the power flux of sunlight is only about 1000 W/m^2 at sea level which requires the solar cell area to be large for even moderate power-consuming equipment [1]. High altitude and high endurance solar-powered RPAs have been developed but are limited to fragile designs capable of handling only small payloads due to the aforementioned power limitations [1]. An alternative energy source to sunlight has been demonstrated on a small scale by the National Aeronautics and Space Administration (NASA) using a laser to illuminate solar panels fixed to the underside of the aircraft [1]. While it is possible to convert laser energy to electricity using conventional solar cells, the greatest efficiency will be achieved when the receiving unit is specifically designed for a particular monochromatic laser source in which case the Photovoltaic (PV) cell is referred to as a Laser Power Converter (LPC).

Using a laser source to transmit power has several advantages over collecting sunlight. Lasers are a more reliable source of energy because they can operate day and/or night and can be directed for optimal incidence angle on a PV cell. Additionally, since certain wavelengths of light are nearly fully transmitted by the atmosphere and clouds, weather conditions would not prevent the delivery of power to the receiving device. Finally, some lasers are capable of outputting power fluxes two orders of magnitude higher than the sun which allows more power to be collected by smaller PV cells [1]. PV cells must have minimal resistance when illuminated by a high power flux since the increasing current magnifies resistive losses. Even with minimal resistive losses, the PV cell operating at a high power flux must be capable of dissipating heat more efficiently than low power flux PV cells. Fortunately, the field of concentrator solar cells provides a significant amount of information about efforts to maintain high efficiency light conversion for high power fluxes.

Concentrator solar cells use an optical system to focus sunlight from a large area to a small solar cell capable of high power output [2]. Previous research has shown that the efficiencies of concentrator cells drop with an increase in area above only a few square millimeters. That, and the higher cost for larger area devices, means that they are typically kept on the order of a few square millimeters [3]. Using concentrator optics to focus laser light onto a small PV cell mounted on an RPA is impractical for several reasons. First, the focusing system would have to be complex enough to quickly adjust its position in order to best capture the incoming laser light as the RPA platform moves through the air unlike concentrator solar cells which require only slow tracking of the sun. Second, the lenses and/or mirrors and the control system necessary for beam alignment contribute additional weight to RPAs that may only be capable of handling small payloads. To avoid the

complications of focusing optics, PV cell areas on the order of a few square centimeters are needed to capture as much of the laser spot as possible after the beam has spread out in propagating over a large distance. Therefore, the drop in efficiency found in previous work for large area devices must be understood and mitigated in designing an LPC large enough for practical applications.

While this work in developing an LPC stems partly from a desire to charge RPAs, lasers are the ideal power carrier to use over distances and under conditions where hardwiring is not possible to support any device for which physically replacing batteries is impractical or dangerous. Some additional applications include remote recharging of unattended ground security sensors and small robots for base force protection. By transmitting power to electric devices, a laser power conversion system can ensure sustained operation and reduce the risk posed to war-fighters responsible for maintaining the equipment. In addition to advancing the development of an operational LPC, this work contributes to future concentrator solar cell development through mitigation of area effects on large area PV cells.

1.2 Concentrator Cells and LPCs

PV cells convert electromagnetic radiation into electricity using a variety of materials and structures to absorb different spectra of light at varying intensities [2]. A continuing effort has been made to find materials and design structures that increase the efficiency of PV cells while minimizing the cost. Most applications of PV cells involve the absorption of broad spectrum sunlight while LPCs can be tailored for efficient absorption of a single wavelength [4]. While multijunction cells have greatly increased the efficiency of solar power conversion, the introduction of multiple absorption layers within a structure increases the cost and complicates the manufacturing process [2]. LPCs, however, can achieve efficiencies over 50% while

maintaining a single junction structure [4]. While the conversion of a monochromatic source provides an advantage in simplifying the junction structure within the PV cell, it presents the additional challenge of operating at power fluxes much larger than typical cells. Fortunately, a significant amount of research has been conducted for concentrator solar cells which operate at power levels more closely resembling those that could be encountered by an LPC.

In order to handle higher intensities of incident light, the cell needs to be able to convert radiation efficiently to electricity while conducting high current densities and quickly dissipating large amounts of heat from the system that can reduce power output or cause damage [2]. Even a 50% efficient PV cell means that nearly 50% of the power is dissipated as heat. Some of the heat comes from the resistive heating that occurs as current from the device encounters resistance traveling through the semiconductor layers and the conducting contact fingers. Additionally, heating results from electron hole recombination which scales with the carrier concentrations [5]. Typically, the absorbing layer where most of the optical generation occurs is at or near the front surface of the cell while the heat is dissipated through the back of the cell. Since the heat has to travel through all of the layer levels before being dissipated, heat extraction is not ideal. One possible method of optimizing heat extraction is moving the absorbing layer closer to the back of the cell by inverting the structure. An inverted structure has the light enter through the substrate layer. The inverted design may also make it possible to recess the metal finger grids used to extract current which allows them to have higher height/width aspect ratios and larger cross-sectional areas which reduces the resistive loss in the grid metal.

1.3 Wavelength and Material Requirements

The first step in determining the structure and materials of the receiving PV cell is identification of the laser source type that will be used as the power transmitter. Three main factors drive the choice of laser source. First, the laser wavelength must lie in a transmission window of the atmospheric transmission spectrum to propagate over large distances with minimal losses. The second factor for consideration is safety. Transmitting power over large distances of uncontrolled environment may present unintended scattering or reflection sending some of the laser energy in the direction of bystanders. In order to reduce the potential hazard posed to operators and bystanders, an "eye safe" laser wavelength is necessary, operating at wavelengths above 1400 nm for which the lens of the human eye absorbs most of the radiation and does not focus the light onto the retina. The third factor is commercial availability of the laser source. High efficiency commercial off-the-shelf lasers above this wavelength are limited to 1550 nm which also lies in the Near-Infrared (NIR) atmospheric transmission window at about $1.4 - 1.8$ μm [6]. Photons from a 1550 nm laser have energies of 0.8 eV so the material used in the LPC must have an equivalent bandgap energy.

A group at Spire Corp. [4] has reported on an LPC cell working at 1315 nm based on an Indium Gallium Arsenide (InGaAs) $In_{0.53}Ga_{0.47}As$ with a bandgap near 0.75 eV. This device should therefore also work as a 1550 nm LPC [7]. Additional work has demonstrated Indium Phosphide (InP) as an effective substrate for lattice-matching InGaAs in Thermophotovoltaics (TPV) [8]. As a suggested means of achieving the desired bandgap of 0.8 eV while maintaining a lattice match to an InP substrate, aluminum can be added to form the quaternary alloy indium aluminum gallium arsenide ($In_{1-x}Ga_xAl_{1-y}As_y$) [7]. Precisely matching the band gap energy to the photon energy is critical in increasing the efficiency of the

LPC [9]. If the bandgap is too high, the photons will not be converted. If the bandgap is too low, the excess photon energy will become heat within the cell, hindering operation and causing damage if not dissipated by other means [1].

1.4 Problem Statement and Scope

The concept of laser power transmission has been explored using silicon and other materials but there are no large area high power PV cells currently available capable of converting 1550 nm light [10]. There is an on-going effort at the Air Force Research Laboratory (AFRL) to develop and optimize a baseline InGaAlAs/InP large area high power PV cell. The cell design goal is to handle power on the order of $10 - 20$ W/cm^2 at an efficiency $\eta > 50\%$. This is an iterative effort that includes modeling, growing the structures using Molecular Beam Epitaxy (MBE), fabricating and testing the PV cells, and then adjusting the design effort according to the test results. In order to contribute to the AFRL effort, this work provides an investigation of resistance sources in an LPC model for different device dimensions further efforts at mitigating power losses.

As previously mentioned, it is expected that scaling to a larger device area will cause a significant drop in efficiency. This drop in efficiency could be caused by series resistance impeding the generated photocurrent as it is drawn from the PV cell. As the area increases, series resistance increases in both the semiconductor layers as they expand laterally, as well as in the metal finger contacts on top of the cell as their length increases [11]. The resistance of these metal finger grids is of great concern in developing large area cells as it leads to excess heat generation and can significantly reduce cell power output [12]. Previous work has demonstrated a significant efficiency when increasing concentrator solar cell area as shown in Figure 1 reproduced from source [3].

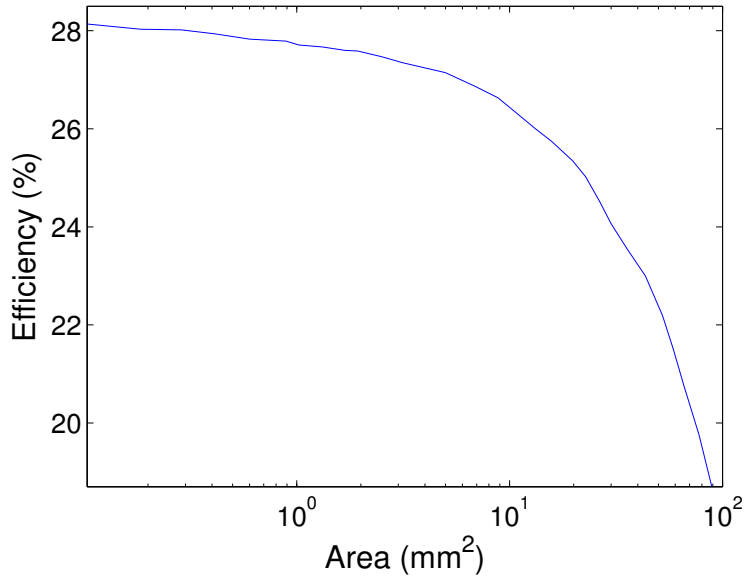

Figure 1. The results of previous research in which a GaAs concentrator solar cell was optimized with an inverted square grid of gold fingers with a finger height of 0.5 μm and finger width of 3 μm under 1000 sun illumination. At each point, a different structure was optimized using variable doping, layer thicknesses and finger spacing. Data from [3].

.

For each area in Figure 1, a different structure was used to optimize the efficiency, preventing the resistive losses from the grid metal, semiconductor layers, and contact resistance from being clearly distinguished in an attempt to characterize and mitigate their contributions. If the efficiency drops significantly as the area is increased by lengthening the device along the direction parallel to the finger contacts while maintaining equal finger spacing, the fingers can be identified as the primary contribution to the drop in efficiency. Fabricating an array of devices with differing finger spacing, lengths, and overall areas could help reveal their relative resistance contributions, but would require significant time and resources. It is more practical to simulate the devices using appropriate simulation software. Synopsys Sentaurus Technology Computer Aided Design (TCAD) software was chosen for this purpose since it can model PV and other semiconductor devices under various illumination schemes.

This work contributes to the on-going AFRL effort by using Sentaurus to compute the efficiency of a three-dimensional GaAs LPC unit cell model while varying the metal finger length and finger spacing. The results show resistive losses can be significantly reduced by increasing the cross-sectional area of the grid metal fingers as well as through the use of a highly doped lateral conduction layer on the top surface of the cell. Using an inverted architecture may allow the thick substrate to be used as the lateral conduction layer. Additionally, high cross-sectional area fingers can be achieved by trenching the substrate with the grid metal pattern and depositing the metal in the trenches rather than depositing them on the top surface.

1.5 Overview

The remainder of this document is organized as follows: First, the theory of PV operation is explained to provide insight into the challenges and solutions involved

in developing PV devices, followed by a discussion of performance parameters that can be used in testing a PV cell's effectiveness under different conditions. Then, a review of previous laser power conversion efforts is explored in the context of rapidly developing general PV technology. Next, the measurement of contact resistance for InP wafers is discussed and related to overall series resistance of an LPC. This is followed by the development of LPC computer models used to predict the performance of LPC models. The simulated performance of two different LPC designs are presented for a variety of different parameter combinations and the results discussed including identification of resistive loss sources. Finally, conclusions and recommendations are presented for the design and fabrication of a large area 1550 nm LPC.

II. Theory

2.1 Single Junction Solar Cell

While solar cell technology has evolved to include a variety of materials and structures, understanding a traditional single junction solar cell is fundamental in understanding and designing more complex devices. The following discussion includes an introduction to the formation of a PN junction diode and its application as a PV device.

PN diode.

The conductivity of a material is determined by the distribution of possible energy levels that can be occupied by the electrons associated with the constituent atoms of the material.

The probability of an electron occupying an energy state for energy E in thermal equilibrium is given by the Fermi function

$$f(E) = \frac{1}{1 + \mathrm{e}^{(E-E_F)/kT}} \tag{1}$$

where E_F is the Fermi energy level, k is Boltzmann's constant and T is the temperature. According to the Fermi function there is a much higher probability of electrons existing in energy levels below the Fermi energy for low temperatures [5].

In a good conductor, the Fermi energy level lies within the conduction band and hence, many electrons have enough energy to escape their atoms thus leaving behind a "holes" where there are effective positive charges. The movement of the free electrons together with the relocation of the holes make up the current flow. In semiconductors without introduced impurities known as dopants, there is an energy gap between the valence and conduction band known as the bandgap and the Fermi

energy level lies between the valence and conduction band such that relatively few electrons are thermally excited into the conduction band.

Pure crystalline semiconductor materials have periodic structures that, along with the atomic properties of the constituent atoms in the lattice, give them useful electronic properties that are exploited for a variety of small and large devices. A crystalline semiconductor that contains no impurities (intrinsic) will have an equal number of electrons in the conduction band and holes in the valence band when it is in thermal equilibrium. That is, the electron concentration n_o is equal to the hole concentration p_o which are equal to the intrinsic carrier concentration n_i. The intrinsic carrier concentration is dependent on the temperature of the structure and is given by

$$n_i = \sqrt{N_C N_V} \mathrm{e}^{(E_V - E_C)/2kT} = \sqrt{N_C N_V} \mathrm{e}^{-E_G/2kT} \tag{2}$$

where N_C and N_V are the effective densities of state of the conduction-band and valence-band respectively, E_V and E_C define the top of the valence band and the bottom of the conduction band respectively, and the bandgap energy, E_G, is given by $E_G = E_V - E_C$ [5].

The conductivity of a material is given by

$$\sigma = q\mu_n n + q\mu_p p \tag{3}$$

where q is the elementary charge, μ_n and μ_p are the electron and holes mobilities in the material respectively and n and p are the electron concentration in the conduction band and hole concentration in the valence band respectively [5].

Since the conductivity depends partly on the carrier concentration, the conductivity of a material can be altered by introducing impurities into the crystal

lattice known as dopants. Figure 2a shows a lattice of GaAs where the gallium has three valence electrons and the arsenic as five valence electrons. By sharing electrons, thereby forming covalent bonds, the outer electron shell of each atom is filled with a total of eight electrons. An n-type dopant, also known as a donor is an atom with an excess of valence electrons such that it can easily be ionized and donate a mobile electron to the lattice. A p-type dopant, also known as an acceptor, is one which can easily accept an electron to become negatively ionized to contribute an excess hole to the lattice [5]. For example, when Tellurium is added into the GaAs lattice as shown in Figure 2b, it has five electrons in its outer shell. Since only four are used in covalent bonds within the lattice, there is an extra electron with energy at the donor energy level which is typically close to the conduction band within the lattice. This additional electron can easily be thermally excited into the conduction band and act as a mobile charge carrier within the material, now considered n-type for it contains a greater concentration of electrons in the conduction band than holes in the valence band. Thus, electrons are the majority carrier of charge. A similar situation arises when a p-type dopant is introduced into the lattice as in Figure 2c. However, this p-type dopant has one fewer electron than necessary to complete the covalent bonds with the surrounding atoms and thus contributes an excess hole, a positive charge carrier, and the material becomes p-type.

A single junction solar cell is created by the junction of a p-type and an n-type semiconductor. Since there are excess holes in the p-type region and excess electrons in the n-type region, there is a density gradient of each type of carrier at the interface. Due to this density gradient, the electrons diffuse into the p-type region and the holes diffuse into the n-type region. This diffusion leaves the ion cores near the interface without their excess hole or electron and thus forms the “depletion

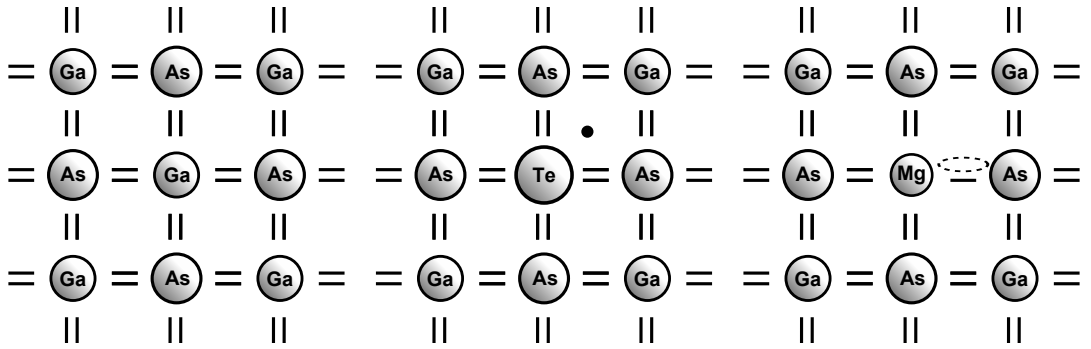

(a) Intrinsic lattice **(b) N-type doped lattice** **(c) P-type doped lattice**

Figure 2. Plane of a GaAs lattice showing the group III Ga sharing its three valence electrons with the five from group VI As to form covalent bonds with 8 electrons per atom. The intrinsic lattice without any impurities is shown in (a), the n-type lattice with a Tellurium atom that has an extra electron is shown in (b), and the p-type lattice with a Magnesium atom that is lacking one electron and thus contributes a hole (c).

region." The ion cores that remain in the depletion region are no longer charge neutral and an electric field forms in the depletion region from the positively charged atoms in the n-type region and negatively charged atoms in the p-type region. The electric field causes holes to move in the direction of the field and electrons to move against it in what is known as carrier drift. The drift direction is opposite the diffusion direction and equilibrium is reached when the two are equal [5]. Figure 3 shows the junction along with the directions of diffusion and drift.

The energy band diagram of the junction is shown in Figure 4 assuming the bandgap energy is constant across the junction. The electric field presents an effective potential that electrons drift down and holes drift up. An external electric field can be introduced such that the cell is "biased." An external electric field in the opposite direction of that formed in the depletion region effectively lowers the energy barrier to carrier transport making it easier for carriers to diffuse and is called a forward bias. A reverse bias is an applied electric field that increases the

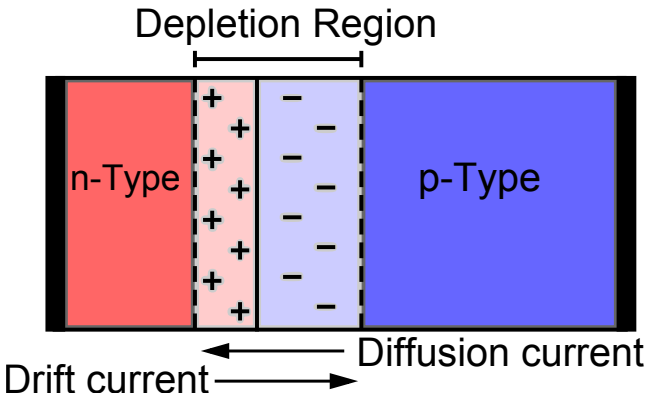

Figure 3. Junction of a p-type and n-type semiconductor. The density gradient at the interface causes hole to diffuse to the n-type region and electrons to diffuse into the p-type region. An electric field forms between the charged ion cores left behind. The presence of the electric field causes a drift current opposing the diffusion, reaching an equilibrium.

potential difference formed at the depletion region making diffusion more difficult but allowing carrier transport via drift.

Photovoltaic Effect.

A photocurrent can be created when incident light excites more electrons out of the valence band into the conduction band, creating more electron hole pairs. The energy of a photon depends on its wavelength by the relation $E = hc/\lambda$ where c is the speed of light, h is Planck's constant, and λ is the wavelength. The energy required to free the electrons from the valence band to the conduction band is the bandgap energy and thus, when the incident photons of light have energy greater than the bandgap energy, an electron-hole pair is generated. The electron is pushed toward the n-type region by the built in electric field of the junction and the hole is pushed in the direction of the p-type region, increasing the drift current within the device and generating what is known as the photocurrent. The increase in electrons in the n-type material and holes in the p-type material creates a secondary electric

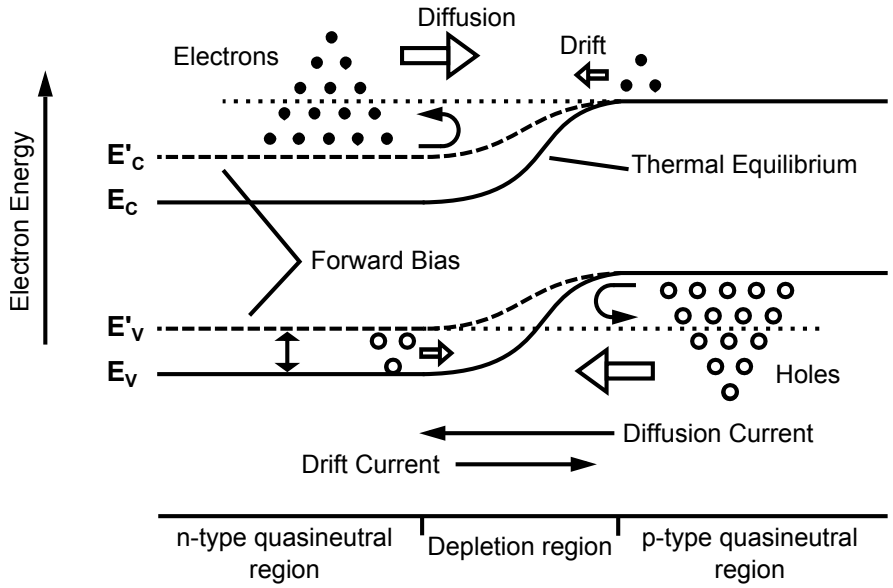

Figure 4. Band diagram of the PN junction shown in figure 3 with a forward bias applied. The forward bias lowers the potential barrier and makes it easier for the diffusion of electrons into the p-type region and holes to diffuse into the n-type region.

field opposing that formed at the junction much like a forward bias would. The reduction in the electric field makes diffusion easier and thus a new equilibrium is reached. The current extracted from the device is then the photocurrent minus the forward bias diffusion current. When there is no external bias, the resulting current is called the short circuit current [13].

Current alone, does not equate to power. Joule's law relates power, P to both the current, I, and voltage, V by $P = IV$. Applying a forward bias allows the electrons to gain potential energy as they drift in the photocurrent. This potential energy can be used to power a load. The forward bias, however, makes diffusion easier and as the voltage of the bias increases the diffusion of carriers reduces the photocurrent. The characteristics of the output current with respect to voltage are discussed further in the two diode model section.

Two Diode Model.

The behavior of the solar cell described in the previous section can be modeled by an equivalent circuit consisting of a current source and two diodes in parallel. The first diode represents the effect of recombination current in the quasi-neutral region (outside of the depletion region) and the second represents that in the depletion region [13]. Manufacturing defects also lead to an alternate path for current in the cell modeled by a resistor in parallel with the diode, known as a shunt resistance, which robs the load of current. Ideally, there would be no alternate paths for current in which case, the shunt resistance would be infinite. Additionally, the solar cell has intrinsic series resistance throughout the cell including the semiconductor layers and the metal grid used to extract the current. This series resistance impedes current flow to the load and reduces the power output of the cell. The combination of these effects are taken into account when the PV cell is represented by the equivalent circuit shown in Figure 5.

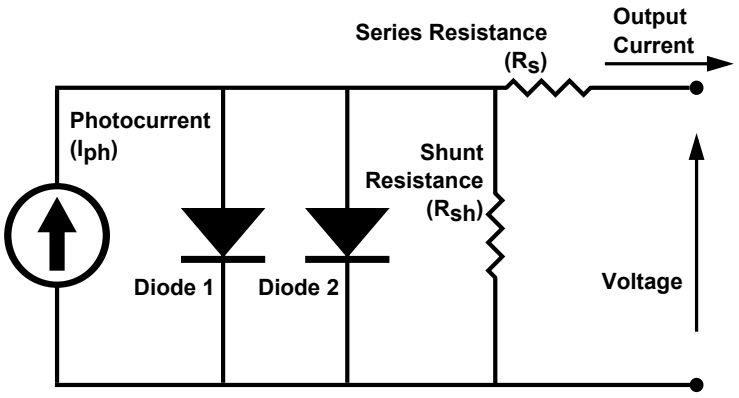

Figure 5. Equivalent circuit of a Photovoltaic cell. The output current of the cell is partly dictated by the values of the series and shunt resistances. The current can be diverted through the shunt resistor and thus, higher shunt resistance values are preferred. The output current is impeded by the series resistance and therefore, lower series resistance values are preferred. Current does not flow through the diode until a sufficient voltage is applied across it [13].

The output current of the equivalent circuit is governed by Equation 4.

$$I = I'_{SC} - I_{o1}(\mathrm{e}^{q(V+IR_s)/kT} - 1) - I_{o2}(\mathrm{e}^{q(V+IR_s)/2kT} - 1) - \frac{V + IR_s}{R_{sh}} \tag{4}$$

where I is the current extracted from the PV cell or delivered to the load, I'_{SC} is the short-circuit current without any resistances in the circuit, V is the external bias voltage, R_s is the total series resistance, and R_{sh} is the shunt resistance [13]. The exponential terms represent the diode behaviors with I_{on} known as the reverse bias saturation current, T is the temperature of the device. The maximum output current occurs at zero voltage and decreases as the voltage increases. Equation 4 shows that increasing the series resistance and/or reducing the shunt resistance allows the current to drop more rapidly with increasing voltage.

The effect of the series resistance on the current-voltage (IV) curve of a PV cell are shown in Figure 6. As the series resistance increases, the "knee" in the IV curve is pushed to lower current and lower voltages. The power generated by the device is given by $P = IV$ so that as the knee shifts, the max power decreases. The Fill Factor gives some measure of how far the IV curve is shifted from its ideal value and is discussed further in Section 2.4 on performance parameters.

2.2 Recombination

While electrons and holes are transported in the semiconductor, there is probability that electrons or holes will recombine non-radiatively with fixed charge centers, other mobile carriers, or crystal defects. Recombination can take several forms. In radiative recombination, the electron releases energy by radiating a photon such that it directly relaxes back to the valence band. Shockley Reed Hall (SRH) recombination involves an intermediate energy level in the forbidden region between the valence and conduction band. The electron relaxes to the intermediate

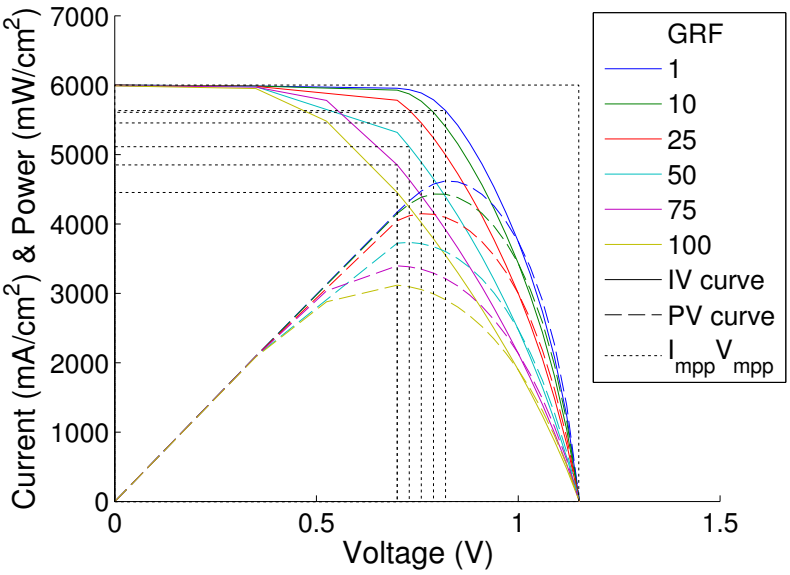

Figure 6. Example Current/Voltage curve of a PV cell demonstrating the effect of series resistance. As the resistivity of the grid metal was increased by a factor (GRF), the IV curve shifted toward the origin. The rectangles extend from the origin to the maximum power points (mpp) on the IV curves. The Fill Factor (FF) gives the ratio of $I_{mpp}V_{mpp}$ to the product of the short circuit current and the open circuit voltage, $I_{sc}V_{oc}$, depicted by the largest rectangle.

energy level via radiation and then further to the valence band via another radiative process. In Auger recombination, an electron in the conduction band transfers its energy to another electron in the conduction band as it relaxes to the valence band. The secondary electron receiving the excess energy is excited further into the conduction band where it will release thermal energy gradually to return to the edge of the conduction band. The three recombination events are shown in Figure 7

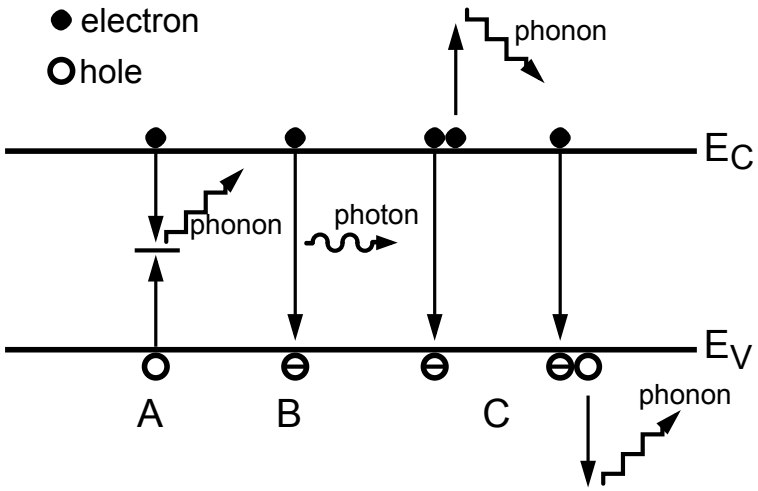

Figure 7. a) Shockley Read Hall recombination in which electrons and holes recombine in mid-level traps within the forbidden energy region which are typically due to defects. b) Radiative recombination in which an electron releases energy in the form of a photon as it relaxes into the valence band. c) Auger recombination in which an electron donates its energy to another electron in the conduction band which then must release energy thermally (in the form of a phonon). The process can also occur in which a hole gives energy to another hole, pushing it deeper into the valence band. It then releases energy in the form of phonons to return to the band edge.

2.3 Window and Back Surface Field

In addition to recombination events within the bulk material, there is recombination that occurs at material interfaces and edges. At these edges and

interfaces, there is a termination or transition in the lattice structure. This introduces additional energy states known as surface states in between the valence and conduction band acting as traps for charge carriers. When electrons or holes recombine by transitioning to or through these energy levels the event is known as surface recombination [13]. In order to reduce the amount of surface recombination additional semiconductor layers are added to "passivate" the surface. For single junction solar cells or LPCs, the top passivating layer is known as the window and the back passivating layer is known as the Back Surface Field (BSF). The lattice constant of the window layer must be well-matched to the underlying emitter layer and with a much higher bandgap to reduce optical absorption within the window. The window may also have a large positive band offset from the emitter so that it acts as a potential barrier for minority carriers [13]. The BSF layer has similar requirements such as lattice-matching the base, a large bandgap, and a large negative band offset from the base.

2.4 Performance Parameters

Many of the performance parameters of a PV device can be extracted from the IV curve. When there is no voltage bias on the cell, the measured current is given by the short-circuit current, I_{sc}. This is the maximum current that can be extracted from the cell. As the cell is biased, the extracted current drops. At a high enough voltage, the extracted current drops to zero, where the IV curve intersects the voltage axis. The voltage at which this occurs is known as the open-circuit voltage, V_{oc}. The power delivered by the cell at any point on the curve is found by the multiplication of the current and voltage values. Thus, the absolute theoretical power limit is found by multiplying the short-circuit current by the open-circuit voltage. In actuality, the IV curve will never extend to this point due to the curved

diode-like response and the resistance effects in the cell. Thus, plotting the power as a function of voltage, the maximum power will lie at a lower voltage than the open-circuit value where the current is just beginning to drop off. The resistances in the cell will force the actual maximum power away from its theoretical limit. A measure of this shift is given by the Fill Factor (FF). The FF is found by dividing the actual maximum power value by the theoretical limit,

$$FF = \frac{I_{mpp}V_{mpp}}{I_{sc}V_{oc}} \tag{5}$$

where the subscript *mpp* indicates the value at the maximum power point.

Another important performance parameter of the cell is the efficiency. There are, however, a number of different types of efficiency. Photons incident on the PV device are converted into carriers that make up the current. The ratio of incident photons to generated carriers is called the Quantum Efficiency (QE). The External Quantum Efficiency (EQE) takes into account the loss of photons due to reflection or other methods of absorption. The Internal Quantum Efficiency (IQE) takes into account only those photons which make it through any optical loss processes. The quantum efficiency is typically represented as a function of incident photon energy or wavelength since the reflection and transmission of photons as well as the conversion of photons to carriers are all related to the complex index of refraction which is wavelength dependent [14].

The energy conversion efficiency of the cell, η, is a measure of the actual maximum power of the cell compared to the incident power on the cell, which is given by the intensity of the source multiplied by the illuminated surface area. Maximizing the energy conversion efficiency or increasing the maximal attainable FF is the primary goal of much of the research in PV technology. This research

specifically explores how mitigating the effects of series resistance can increase the fill factor and allow higher efficiencies to be maintained for large area LPCs.

2.5 Series Resistance

In order to attach the aforementioned junction structure into a circuit, electrical contact must be made. Figure 8 shows the layer stack complete with metal contacts on the top and bottom of the cell. In traditional architectures, the entire back surface of the device is covered in a conducting metal to form one contact. The other contact is created on top of the cell by placing metal fingers in a grid pattern on top of the cap layer.

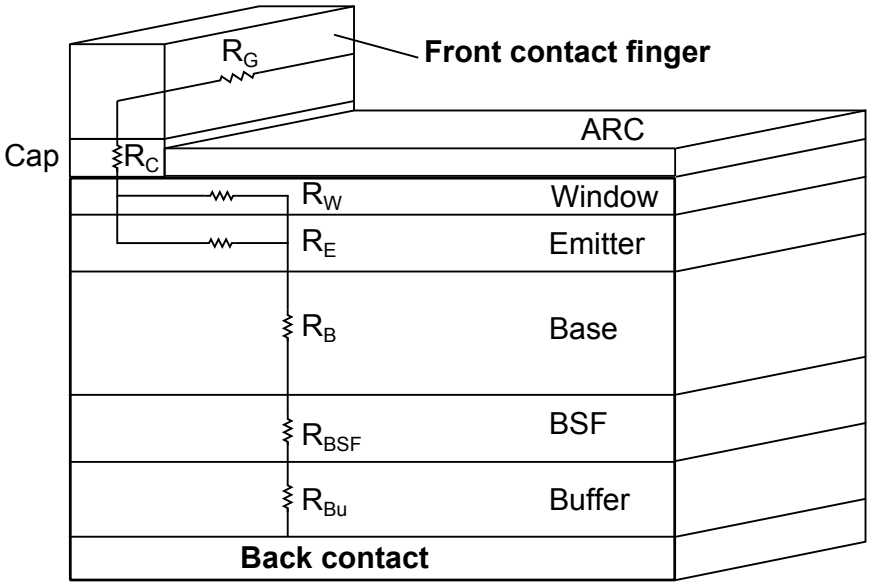

Figure 8. Section of a single junction PV cell showing the current flow resistances. In this simplified model, carriers are assumed to flow vertically to the emitter and window layers and then laterally to the grid metal contact for extraction. The primary contributions to the series resistance are in the grid metal and the window and emitter layers. Knowing the relative contributions is critical for devising methods of mitigating series resistance.

The current must travel through multiple semiconductor layers before reaching the metal contacts connected to a receiving battery or device. The current experiences resistance en route through what is know as the series resistance of the cell which reduces the current output. The total series resistance is the sum of resistances in the various layers and contacts of the cell. Figure 8 shows the contributing resistances in the cell where the total resistance is given by

$$R_s = R_G + R_C + R_L + R_B + R_{BSF} + R_{Bu} \tag{6}$$

where R_G is the resistance of the front grid metal, R_C is the resistance of the cap layer, R_B is the resistance of base, R_{BSF} is the resistance of the back surface field, R_{Bu} is the resistance of the buffer, and R_L is the combined resistance of the window and emitter layers given by

$$\frac{1}{R_L} = \frac{1}{R_E} + \frac{1}{R_W} \tag{7}$$

where R_E is the resistance of the emitter layer and R_W is the resistance of the window layer.

While the sources of resistance are well known, the relative contributions to the total resistance have not yet been fully explored and depend on the structure and materials used. Some attempts at characterizing the resistance contributions are discussed in the following chapter.

2.6 Analytic Model

When current is passed through a resistive material such as the layers in the device and the grid metal, energy is lost. This loss is known by several names including Joule heating, resistive heating, ohmic heating and I^2R loss since the

power lost is given by $P = I^2R$. When voltage is applied across a device, as it is in a PV cell, an electric field is formed. Electrons in the medium, gain kinetic energy as they are forced from low to high potential (due to their negative charge). Electrical current is the representation of the collective movement of electrons in the field. The electrons that make up the moving current occasionally collide with ions in the material and transfer their kinetic energy. The kinetic energy becomes vibrational energy in the ions which is considered heat. Losses due to Joule heating are a concern in many electronic devices and drive the need for thicker wires and higher voltages when significant current is moved through the system.

An analytical model borrowed from Gress and Varlamov [11] serves as a starting point for determining the relative contributions of the finger and the window/emitter layer to the resistive losses . Figure 9 shows a top down perspective of a single finger connected to a bus in which all of the current is assumed to flow perpendicular to the length of the finger in the window/emitter layer toward the finger. The simplest way to increase the area of the device is to increase the finger spacing, S, and the finger length, L_f, and keep the bus bar the same. Hence we will neglect the bus bar contributions by assuming that $S >> W_f$ and $L_f >> W_b$ where W_f is the finger width and W_b is the bus width.

To find the resistive loss in the two sections, both the resistance and current values are needed. Starting with the window/emitter layer, the resistance is found by

$$R_e = \frac{\rho_e dx}{L_f} \tag{8}$$

where ρ_e is the sheet resistivity of the window/emitter layer. The current moving through the sheet at position x is given by

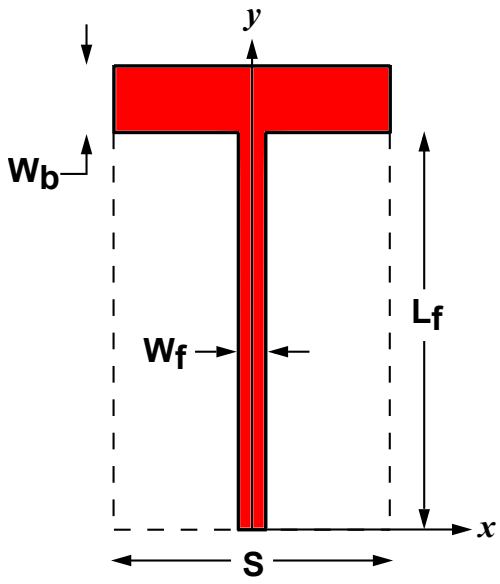

Figure 9. Top down perspective of a single metal finger connected to a bus where W_b is the bus width, W_f is the finger width, L_f is the finger length, S is the finger spacing. It is assumed that $S \gg W_f$ and $L_f \gg W_b$ and current is assumed to move perpendicular to the finger length in the window/emitter layer.

$$I(x) = JL_f(S/2 - x) \tag{9}$$

where J is the current density extracted from the device and S. The I^2R power loss in the sheet per unit area is then

$$\bar{P}_e = \frac{2}{SL_f}\int_0^{S/2}(JL_f(S/2-x))^2\frac{\rho_e}{L_f}dx = \frac{\rho_e S^2 J^2}{12} \tag{10}$$

The resistance in the metal finger is

$$R_f = \frac{\rho_f}{W_f H_f}dy \tag{11}$$

where ρ_f is the bulk resistivity of the metal. The current at position y along the finger is given by $I(y) = yJS$. Therefore, the I^2R power loss in a segment dy of the finger is given by

$$I^2R = (yJS)^2 \frac{\rho_f dy}{W_f H_f} \tag{12}$$

and the total power loss in the finger per unit area is given by

$$\bar{P_f} = \frac{1}{L_f S} \int_0^{L_f} (yJS)^2 \frac{\rho_f}{W_f H_f} \, \mathrm{d}y = \frac{\rho_f S J^2 L_f^2}{3 W_f H_f} \tag{13}$$

Equation 10 shows that the power loss in the window/emitter layer is expected to show no dependence on the finger length but increase quadratically with the finger spacing. Equation 13, however, shows that the power loss in the fingers is expected to show a quadratic dependence on the finger length and a linear dependence on the finger spacing.

In developing a large area LPC, the exact causes of series resistance will be explored by altering the structure with the intent of mitigating the effects of resistance. The analytic model suggests that increasing the height and width of the finger, along with decreasing the finger spacing would significantly reduce the resistive losses. However, increasing the width or decreasing the spacing means the fingers will cover a larger area of the front surface. Since the metal fingers can reflect and absorb most of the light, they reduce the amount of light that penetrates into the absorbing layers where optical generation occurs. For instance, gold reflects about 98% of normally incident light at 1550 nm [6]. Taller fingers also block more light for anything other than a normal incidence angle. This type of loss resulting from blocking incident light from penetrating into the semiconductor layers is known as shadowing loss and must be carefully balanced in mitigating resistive losses.

2.7 Shadowing losses

The shadowing loss is a function of the front grid finger dimensions, the grid spacing and the angle of incidence of the light. Figure 11 shows how the finger blocks the incident light from reaching the semiconductor layers.

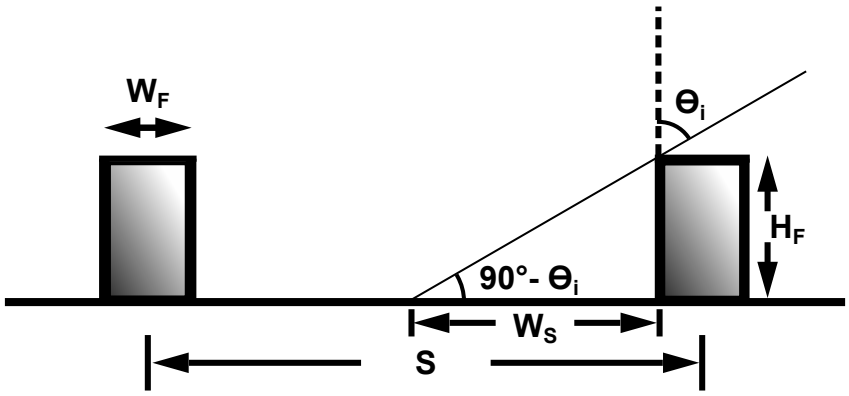

Figure 10. Shadowing of the semiconductor layers by the grid metal fingers where W_F is the finger width, H_F is the finger height, W_S is the shadow width, S is the finger spacing, and θ_i is the incidence angle of illumination.

For a cell with parallel fingers spanning the entire top surface in which the plane of incidence is perpendicular to the length of the fingers, without considering diffraction, the percentage of light lost due to shadowing, L_s is given by

$$L_s = 1 - \left(\frac{H_f}{\tan(90^\circ - \theta_i)} + W_f \right) \frac{1}{S} \tag{14}$$

where H_f is the finger height and θ_i is the incidence angle of illumination. Figure 11 shows the shadowing loss percentage for a PV cell with a parallel grid illuminated at normal incidence (such that finger height can be ignored) as a function of the grid spacing.

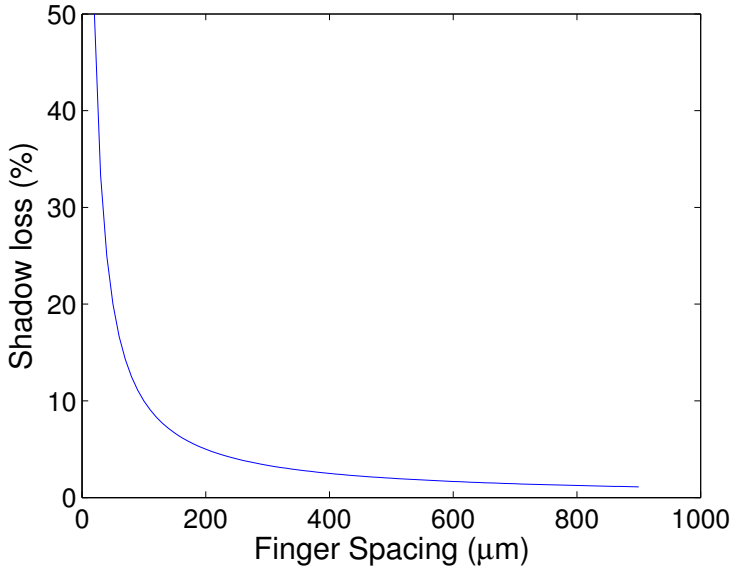

Figure 11. The percentage of power loss due to the shadowing of the grid metal fingers at normal incidence angle of illumination for a finger width of 10 μm**.**

Since the resistive losses increase with grid spacing and the shadowing losses decrease with grid spacing, the grid must be optimized according to the sheet resistance of the PV device. Additionally, equation14 shows that any methods of increasing the finger cross-section to reduce the resistive losses must take the increased shadowing losses into account.

2.8 Contact Resistance

In addition to resistance in the bulk regions of semiconductor and grid metal, each interface between two different materials has an effective resistance known as contact resistance. If two metal contacts are created on a sheet of semiconductor material, a current flowing between them will experience both the specific contact resistivity (ρ_{sc}) and the sheet resistance (R_{sheet}). If the metal contacts are separated by a distance x, the resistance between the contacts is estimated by

$$R = 2\rho_{sc}/(w^2) + xR_{sheet}/w \tag{15}$$

where w is the width of the metal contact pads and therefore, the width of the transmission line between them. In order to measure the sheet and contact resistance, an array of metal contact pads can be deposited with varying distances between them. Then, the total resistance between two adjacent contacts can be determined by applying a voltage difference and measuring the through current. The total resistance is found between each of the contact pads and plotted as a function of the distance between the contact pads used in each measurement. Fitting Equation 15 to the resulting resistance plot is then used to solve for the desired parameters ρ_c and R_{sheet}. This method for determining the contact and sheet resistivities is known as the Transmission Line Method (TLM).

2.9 Cell Inversion

Heat Extraction.

In a traditional solar cell, the semiconductor layers are grown on a thick substrate through Metalorganic Chemical Vapor Deposition (MOCVD) or Molecular Beam Epitaxy (MBE). An inverted PV cell differs from conventional cells in that light enters through the transparent substrate layer. The inverted design moves the solid metal anode contact to within a few microns of the light absorption layer (as opposed to ≈ 300 μm in the non-inverted design). This solid metal contact covers the entire bottom of the cell and can be soldered directly to a heat sink for heat extraction.

Recessing Metal Fingers.

The metal contact on the top surface of the cell is created by depositing metal fingers. The fingers need to be sufficiently large and closely spaced to carry the generated current while not being so large or so close as to block a significant amount of light incident on the device from reaching the absorbing layer. The finger spacing is often near 200 μm for concentrator solar cells operating at 1000 suns [13]. Various techniques have been used to create fingers with high height/width aspect ratios that do not block significant amounts of light. For normal incidence, the shadowing losses of high aspect ratio fingers are the same for low aspect ratio fingers of the same width but the higher aspect ratio fingers present a lower resistance. Even at an angled incidence, as long as light hitting the sides of the fingers is reflected back into the semiconductor layers with minimal absorption or upward scattering, then the high aspect ratio is more desirable.

Typical fingers on concentrator cells have widths of 5 μm and height/width aspect ratios near $0.6 - 1$ [13]. However, using photolithography/evaporation/lift-off, fingers with widths near 3 μm with aspect ratios of more than two can be achieved [13]. The additional processing steps make the achievement of high aspect ratios difficult to achieve when the grid fingers lie on top of the surface [3]. Also, the further they extend from the top of the device, the more complicated it becomes to apply anti-reflection coatings and the more the fingers will shadow the device except at normal incidence. One method of increasing the aspect ratio can be achieved by recessing the metal fingers.

Nickel fingers have previously been recessed within silicon solar cells using a laser to make grooves on the surface of the cell [15]. The so called Buried Contact Solar Cell (BCSC) demonstrated record efficiencies at the time of its introduction but the development of more simple metallization techniques that could easily be

scaled for mass production such as screen printing, laser ablation, and electroplating led research away from buried contacts [15] [13].

In addition to improving heat extraction capabilities, inverting the design moves the thick substrate layer to the top of the device. This layer is sufficiently thick to allow high aspect ratio fingers to be recessed into the surface. As the cross-sectional area of the metal contacts increases, the resistance decreases but the shadowing increases and vice versa. By inverting the cell from traditional designs such that the light enters through the substrate, it may be possible to recess the metal grid fingers and increase their cross-sectional area. Recessing the metal fingers may additionally allow some of the light blocked or scattered by the fingers to remain in the semiconductor layers for absorption, thereby reducing the shadowing losses.

III. Background

Within the vast body of research conducted related to photovoltaic technology, there are relatively few efforts that relate to the design of an LPC. This section discusses relevant findings to date. First, laser power transmission systems are discussed in terms of their feasibility and current working status. The importance of the receiving photovoltaic used in laser power transmission is highlighted and leads into a discussion of current monochromatic solar cells and laser power converters. This is followed by an exploration of concentrator solar cell research, specifically that which provides insight into the causes of and possible mitigating techniques associated with resistive power losses.

3.1 Power Transmission Efforts

In a recent dissertation, Raible [10] discussed the possibility of combining free space optical communication and laser power transmission. The photodetecting receiver used to explore free space optical communication consisted of an array of nine silicon solar cells. While the 1.1 eV band gap of silicon is not optimal for 1550 nm laser power conversion, the research acted as a proof of concept and revealed challenges to achieving theoretical efficiency [10]. The performance of a single Vertical Multi-Junction (VMJ) silicon cell was tested using laser wavelengths of 808 nm, 940 nm, and 976 nm and the peak power outputs were 4.68 W, 6.83 W, and 7.24 W, and for an impinging optical power of 25.87 W [10]. The band gap of silicon is near 1.1 eV and as expected, this previous work demonstrated the importance of using photon energies near the band gap of the receiving cell. The 976 nm laser, with photon energies of 1.27 eV was best suited to the band gap of

silicon than the 808 nm or the 940 nm sources which have photon energies of 1.53 eV and 1.32 eV respectively.

Previous work with silicon cells also demonstrated that the efficiency of a PV can be reduced when it is not uniformly illuminated. Partial illumination leads to non-uniform optical generation and an imbalance of charge carrier densities. This imbalance causes current to flow from the areas of high illumination to areas of low illumination in what is known as cell back-feeding. This process detracts from the current output and the efficiency [10]. This phenomenon will have to be explored when testing LPC designs.

3.2 Overview of LPCs

InGaAs and InAlGaAs Cells.

Photovoltaic cells have been designed previously with the goal of converting laser light at a specific wavelength. In 1993, the Spire Corporation designed single junction $In_{0.53}Ga_{0.47}As$ cells grown on an InP substrate and predicted their power conversion ability using the results of illuminating the cells with AM0 solar spectrum and finding the external quantum efficiency at a wavelength of 1315 nm [7]. The cells were circular with radial front metal grid lines and had a diameter of approximately 4 mm. The entire back surface was metallized with thermally evaporated AuZn and the front grid lines were created using electron-beam evaporated Cr/Ag/Au. The resulting fingers were 3 μm $\times$ 3 μm in cross-section. Two different types of cells were fabricated. One design having both a InP window on top of the InGaAs emitter region and a highly doped (10^{19} cm^{-3}) InGaAs cap layer between the window and the grid metal. The other design omitted these two layers, having the grid metal directly on top of the emitter. Both cells had a quarter-wave Si_3N_4 anti-reflection coating applied, optimized for 1.315 μm light.

The efficiencies of the cells under 5.57 W/cm^2 illumination of a 1.315 μm source were estimated to be 29% based on the open-circuit voltage and fill-factor of the AM0 illumination tests (484 mV and 66.8% respectively) and a measured external quantum efficiency of 86% at 1.315 μm. The cells with the InP windows had a higher average efficiency of 13.2% for concentrated light (average of 90 AM0 suns) compared to the windowless cells which had an average efficiency of 8.91% (average of 102 AM0 suns). The difference was attributed to the ability of the highly doped InP layer to lower the series resistance in the cell by lateral conduction of the generated current. The InP also passivated the surface of the emitter, thereby reducing the surface recombination rate of the otherwise exposed InGaAs emitter layer.

This work serves as a baseline for future cell design and contains recommendations for the exploration of $In_xAl_{1-x}Ga_yAs_{1-y}$ where x and y represent the fractional concentration of indium and gallium respectively to achieve an optimal bandgap for the desired laser source. This alloy has band gaps approaching 0.8 eV and can be lattice-matched to a InP substrate, making it ideal for the design goal of a 1550 nm LPC [7].

GaAs LPC with Lateral Conduction Layer.

Monochromatic illumination of a GaAs was explored at the Fraunhofer Institute for Solar Energy Systems in Germany with results reported for different illumination wavelengths and intensities [9]. The GaAs structure had a Lateral Conduction Layer (LCL) consisting of a highly n-type doped $Ga_{0.5}In_{0.5}P$. The entire layer stack is given in Table 1. The doping is represented by orders of magnitude with n,n$^+$, and n^{++} indicating donor dopants on the order of 10^{17}, 10^{18} and 10^{19-20} cm^{-3} respectively. The orders of magnitude of the acceptor dopants are indicated with

the letter p and the same superscript convention [13]. The thicknesses of the layers were not reported with the exception of the 400 nm thick LCL.

Table 1. Fraunhofer Institute LPC layer structure [9]

Region	Material	Doping
LCL	$Ga_{0.5}In_{0.5}P$	n^{++}
window	$Ga_{0.5}In_{0.5}P$	n^{++}
emitter	GaAs	n
base	GaAs	p
BSF	$Ga_{0.5}In_{0.5}P$	p^{+}
substrate	GaAs	p

The inclusion of the LCL is motivated by the assertion that the sheet resistance of the emitter layer is the limiting factor of LPCs operating under high illumination intensities and thus, high current densities. The researchers comment that a well-designed grid can reduce ohmic losses but the lateral current flow in the emitter is more significant [9]. The assertion, however, is not cited nor justified further in the paper. Thus, the precise contributions to the ohmic losses of the grid and the emitter must be further explored to advance designs aimed at mitigating the two sources of resistance.

The efficiency of the cell peaked at an illumination wavelength around 830 nm. The researchers conducted further experiments with an 810 nm source. The efficiency reported using the 810 nm source was 53.4% with an illumination intensity of 43 W/cm^2.

Without the LCL, efficiency values were close to 53.4% under conditions where series resistance is minimized. Series resistance is expected to be small in cases where the distance between grid fingers is small and where the finger lengths

themselves are sufficiently short. Thus, a simulation of a GaAs single junction cell under 810 nm illumination having a small surface area was expected to return efficiency values near 50%.

Concentrator Solar Cell Research.

Conventional solar cells are directly exposed to unconcentrated light. Therefore, it is necessary to build vast arrays of conventional solar panels to convert energy on a large scale. Concentrator Photovoltaics (CPVs), however, use either lenses or mirrors to focus sunlight onto a relatively small PV device that has been designed with special consideration given to increased intensity and heating. High efficiency CPVs reduce the consumption and therefore, the cost of the semiconductor material used in creating the device. There are, however, additional costs that arise from the focusing and tracking systems and assembly. Previous research has demonstrated that CPVs must operate at concentrations of at least 1000 suns in order to compete with the cost of traditional cells [16]. At these high concentration levels, the current extracted from the cell increases drastically, thereby increasing I^2R power losses due to series resistance within the cell. This power loss results in an efficiency drop. The series resistance, further explained in Section 2.5, increases as the area of the PV device increases and previous research has shown that a steep drop in efficiency is expected for cell areas above 10 mm^2 under 1000 sun illumination [3]. The drop in efficiency is shown Figure 1 adapted from the results of [3].

The cost per unit of energy of CPVs depends on the manufacturing and installation cost and the efficiency of the devices. Manufacturing and installation costs typically decrease with cell area but the efficiency of the cell decreases with increasing area due to increased operating temperatures and resistive losses [13]. CPV areas are thus designed to minimize overall cost and the sizes are typically

below 1 cm^2. Since CPVs areas are kept low, methods of mitigating series resistance in large area CPVs have not been fully explored. With a design goal of an approximately 6 cm^2 device operating at laser intensities of $10 - 20$ W/cm^2 (100 to 200 suns), the series resistance is expected to cause significant loss. Predicting the sources and amount of that loss is part of the goal of this research.

Researchers at the Solar Energy Institute in Madrid have published a significant amount of work relating to solar cell design optimization [3][16][17]. To investigate the series resistance in concentrator p-on-n GaAs solar cells, a holistic optimization approach was taken, simultaneously optimizing doping concentrations, layer thickness, device area, and shadowing factor. With this approach, the efficiency was predicted as a function of concentration and cell area while varying certain parameters such as front contact resistance [3]. One of the findings pertinent to the goal of designing a large area LPC was the efficiency of a GaAs solar cell with an illumination of 1000 suns as a function of cell area [3]. The results were reproduced in Figure 1. In generating this plot the fixed parameters were a finger width of 3 μm, finger height of 0.5 μm, a finger resistivity of 2.2×10^{-6} $\Omega - cm$ (representing the resistivity of gold), a substrate width of 350 μm, a substrate resistivity of 2×10^{-3} $\Omega - cm$, and resistivities of the front and rear contacts of 10^{-5} $\Omega - cm^2$. For the contact resistance values used, the front contact resistance was shown to be less than the resistance for the front metal grid [3]. The front grid metal was arranged in an inverted square design to minimize the lengths of the fingers. In this design, shown in Figure 12a, only the fingers intersecting in the center of the cell are as long as the device itself. In a parallel configuration shown in Figure 12b, all of the fingers are as long as the device. In both cases, the total amount of shadowing is the same for equal finger spacing. Thus, the inverse square grid provides the benefit of shorter fingers where possible without increasing the shadowing factor. There are,

however, places in the inverted square grid where the distance to a finger increases as a result of corners.

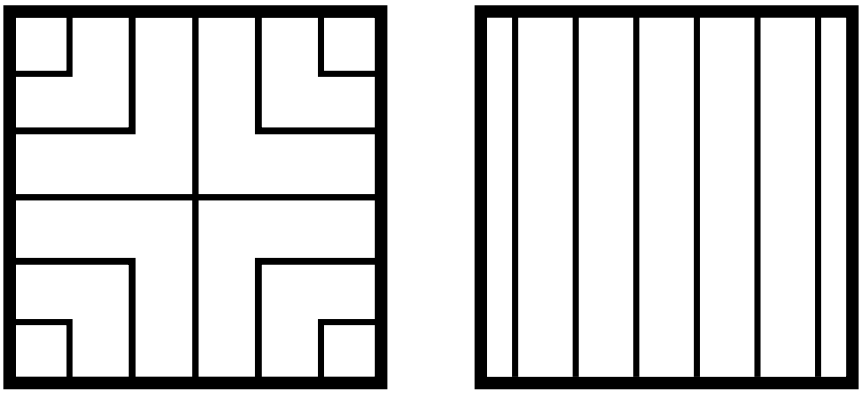

(a) Inverted square grid **(b) Parallel finger grid**

Figure 12. Two configurations of the front contact grid fingers. (a) shows the inverted square design investigated by Algora *et.al* which reduces the average length of the fingers but increases the distance between fingers along the diagonals. (b) shows the parallel finger grid where each finger is the length of the device.

Computer Modeling of Resistance Contributions.

Identifying the contributions from different parts of the cell to the total series resistance is critical in mitigating the I^2R losses and optimizing the design. Previous work has attempted to characterize the sources of resistance in silicon solar cells using semiconductor modeling software. Daliento and Lancellotti used SILVACO ATLAS simulations to model the unit cell of a silicon solar cell [18]. The metal finger used for the model had a cross-section of 10 μm $\times$ 10 μm and was 5000 μm long. Their research sought to compare the performance of the cell under different illumination conditions using a "1D, 2D, and 3D" model. The actual model in all three cases was three-dimensional. In the "1D" case, the whole top

surface of the cell was made a contact for current extraction such that the current flowed vertically within the cell. The "2D" simulation, the metal finger was uniformly contacted such that current could flow laterally in the semiconductor layers toward the finger for extraction. In the "3D" simulation, only the tip of the metal finger served as a contact, thus forcing current to flow through the length of the finger before being extracted. The series resistance in each case was found using the two-illumination method proposed in [12] wherein

$$R_s = |\frac{V_2 - V_{MP1}}{I_2 - I_{MP1}}| \tag{16}$$

Two IV curves are used, each at different illumination intensities. The MP subscript indicates that it is the value at the maximum power point. I_2 is given by $I_{sc2} - I_{sc1} + I_{MP1}$ and V_2 is the corresponding voltage.

The work assumed that the resistance contribution from the emitter region was the difference between the "2D" and "1D" results and the contribution from the metal finger was the difference between the "3D" and "2D" results. The contribution from the emitter region was highly dependent on the emitter junction depth. By comparing the results, they concluded that at low photon concentrations (below about 20 suns) the metal grid resistance was mostly negligible. At concentrations of 100 suns, however, they concluded that the metal finger can contribute around 30% of the total series resistance and the emitter contributes $25 - 40\%$ depending on the emitter depth.

However, the metal finger used in the simulations had a cross-sectional area of 100 μm^2. The analytic model of power loss in the finger discussed in Section 2.6 predicts that the finger width and height play a major role. A 10 μm wide finger presents significant shadowing. As mentioned previously, concentrator cells normally have finger dimensions of 5 μm by $3 - 5$ μm. For a typical concentrator cell then,

the analytic model predicts power losses in the finger under similar conditions to increase by $4 - 7$ times that given by the simulation results. The fingers studied in the work of Algora et. al. in [3] were 3 μm $\times$ 0.5 μm which would present power losses in the fingers of 67 times that given for the silicon solar cell model presented in [18] according to the analytic model presented in 2.6. If it is possible to recess the fingers such that they are 5 μm and 20 μm deep, the losses might be more comparable since the cross-sectional area of the finger would also be 100 μm^2.

3.3 Proposed Baseline Design

The PV cell fabricated by the Spire Corporation discussed in Section 3.2 serves as a starting point design and method for the AFRL large area 1550 nm LPC. Figure 13 shows the Spire design compared to the proposed AFRL baseline design.

The most notable difference in the AFRL design is the use of the inverted architecture which allows the absorbing layer to be close to the heat sink at the bottom of the device and allows the grid metal fingers to be recessed, giving them a higher height/width aspect ratio as discussed in Section 2.9. Through the inversion, the baseline design maintains an n-on-p design in order to try to achieve a low contact resistivity on the n-type substrate. The InP window layer is replaced by an InGaAs spacer layer between the emitter and the cap layer which now contacts the back of the device. The InP buffer is removed and the BSF is grown directly on the substrate before the InGaAs base layer. The bandgap of the InGaAs absorbing layer will also be optimized for 1550 nm conversion rather than the 1315 nm design suggested in [7] possibly using a quaternary structure of InGaAlAs as discussed in Section 3.2.

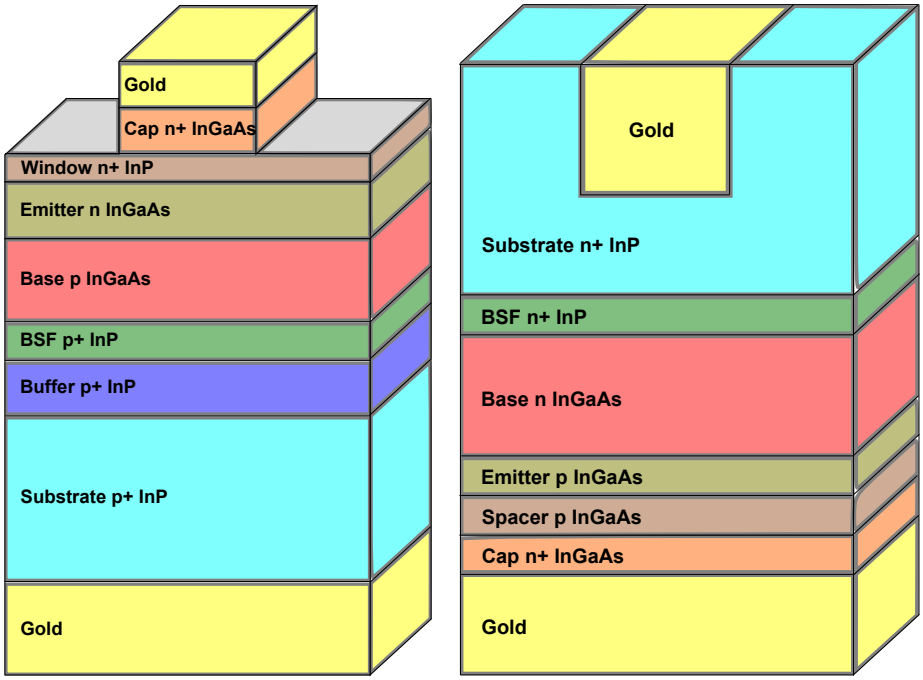

(a) Spire layer stack (b) AFRL baseline design

Figure 13. (a) The layer stack from the Spire Corporation used in [7] and (b) the baseline AFRL design with an inverted architecture and recessed grid metal. The inverted grid allows the absorbing layer to be close to the back contact and heat sink.

IV. Methods

This chapter contains two primary sections. The first section describes the measurement of contact resistance in InP wafers that were similar to the substrates that would be used in a deep trench LPC, shown in Figure 13 (b). The second section explains the development of 810 nm LPC computer models that were used in exploring window/emitter and finger losses.

4.1 Contact resistance

Previous research on CPVs showed that the front contact resistance could dominate the total series resistance values for contact resistances of $10^{-4}\ \Omega - \mathrm{cm}^2$ or higher but could be surpassed by the front grid metal component of resistance if the front contact resistance was lower than $10^{-4}\ \Omega - \mathrm{cm}^2$ [3] [19]. Contact resistance was not included in the simulations described in the following section since the primary focus was to characterize the bulk resistive losses. The simulation results, therefore, are useful only assuming a sufficiently low contact resistance can be achieved in the fabrication process.

The proposed AFRL baseline LPC uses an n-type InP substrate as the top of the device. Achieving a low contact resistivity requires a combination of making informed decisions based on previous research as well as experimental trials. To that end, n and p-type InP wafers were metallized using Ti/Pt/Au to identify the difficulties associated with the process, formulate recommendations for the actual LPC devices and to inform the computer models. The metallization pattern used was a series of contact pads with varying spacings known as transmission line method (TLM) pads designed for contact resistance measurements using the TLM described in Section 2.8.

The preparation of the n and p-type wafers were the same except for the first step used in the photolithography of the p-type wafers. Hexamethyldisilazane (HMDS) was applied to the p-type wafer first to allow the photoresist to adhere. AZ5214 negative resist was spun onto both wafers at 4000 rpm for 30 seconds with a ramp of 200 rpm/sec. The wafers were exposed under the TLM mask for 2.2 sec and then baked at 125 °C for 60 sec. They were then flood exposed for 70 sec and developed for 45 sec with 351 developer. They were then placed in a plasma asher for 2 minutes to remove the remaining resist.

The TLM pads were metallized using electron beam evaporation to deposit Ti, Pt, and Au with thicknesses of 20 nm, 30 nm and 400 nm respectively. Figure 14 shows one individual TLM pad.

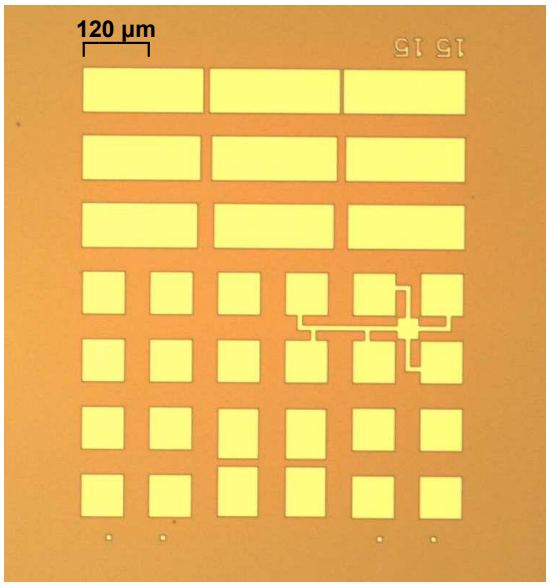

Figure 14. Microscope picture of a gold TLM pad on an InP wafer at 5x magnification. The rectangles are situated with increasing spacing from 5 μm to 30 μm in increments of 5 μm. Current measurements are taken between adjacent rectangles and the resulting data is fit as discussed in Section 2.8 to find the contact resistivity.

The results of the TLM measurement reveal that the quality of contact can be highly variable across the surface of the wafer. Figure 15 shows the measured specific contact resistivity (ρ_{sc}) at different positions on the n-type InP wafer. The positions are given relative to one another because the individual TLM pads were divided into repeating sets of four rather than being uniformly distributed. Figures 16 and 17 show the ρ_{sc} values measured on the p-type wafer that was split into two pieces.

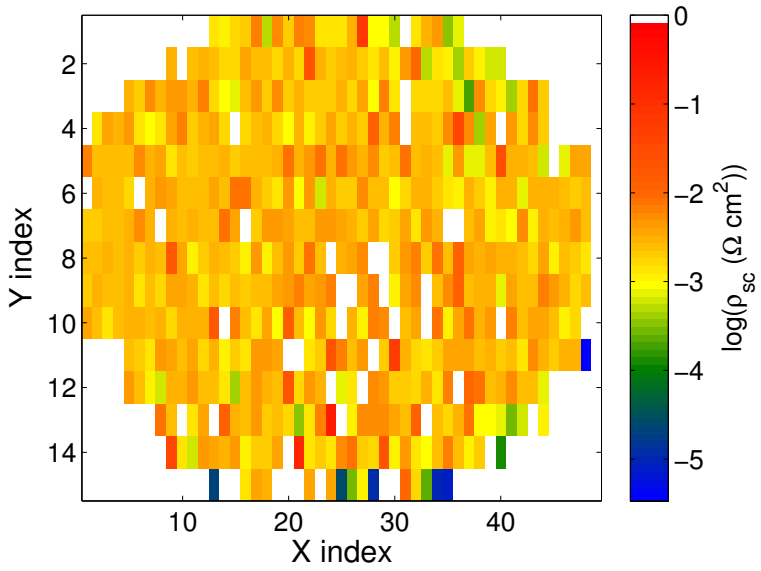

Figure 15. Spatial map of the measured specific contact resistivity of an n-type InP wafer. The zero values hold the position of places that were either not on the wafer or that returned non-physical (negative) values during the TLM measurements. Only 5 of the values were below $10^{-4}\ \Omega - \mathrm{cm}^2$. The axes give relative positions of the TLM pads for each measurement rather than absolute position.

The spatial distribution of ρ_{sc} plotted using a logarithmic scale showed that values below $10^{-4}\ \Omega - \mathrm{cm}^2$ were achieved in only a few places on the n-type wafer and none of the p-type . The overall results are summarized in Table 2.

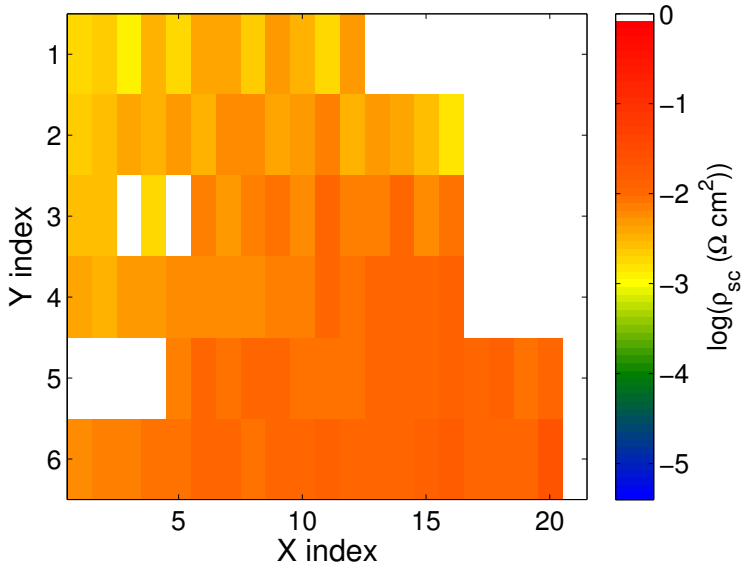

Figure 16. Spatial map of the measured specific contact resistivity of p-type InP wafer piece #1. The zero values hold the position of places that were either not on the wafer or that returned non-physical (negative) values during the TLM measurements. None of the measured values were below $10^{-4}\ \Omega - \mathrm{cm}^2$ and the lowest was $1.3 \times 10^{-3}\ \Omega - \mathrm{cm}^2$. The axes give relative positions of the TLM pads for each measurement rather than absolute position.

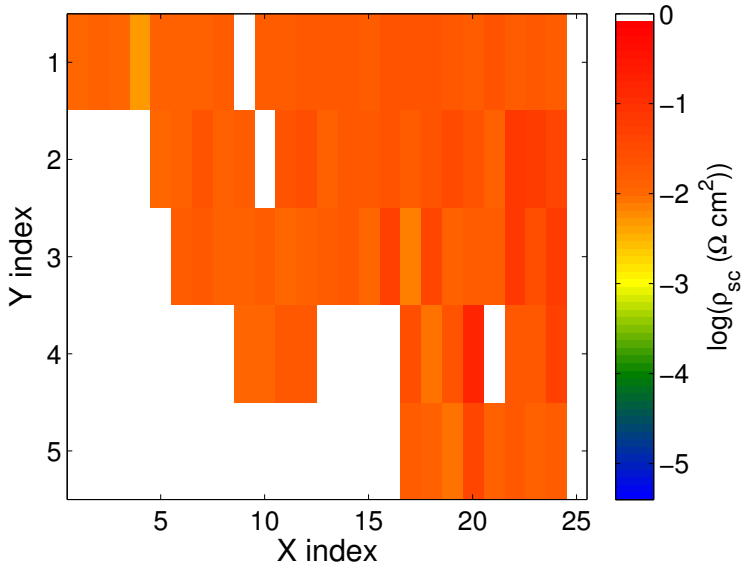

Figure 17. Spatial map of the measured specific contact resistivity of p-type InP wafer piece #2. The zero values hold the position of places that were either not on the wafer or that returned non-physical (negative) values during the TLM measurements. None of the measured values were below $10^{-4}\ \Omega - \mathrm{cm}^2$ and the lowest was $5.0 \times 10^{-3}\ \Omega - \mathrm{cm}^2$. The axes give relative positions of the TLM pads for each measurement rather than absolute position.

Table 2. TLM ρ_{sc} results on InP wafers. All units in $\Omega - \text{cm}^2$

Wafer	Mean	Median	Std Dev	Minimum
n-type InP	6.0×10^{-3}	2.6×10^{-3}	4.4×10^{-2}	3.4×10^{-6}
p-type InP 1	7.1×10^{-3}	7.1×10^{-3}	3.7×10^{-2}	1.3×10^{-3}
p-type InP 2	2.3×10^{-2}	1.7×10^{-2}	2.17×10^{-2}	5.0×10^{-3}

Most of measurements yielded ρ_{sc} values at or above $10^{-3}\ \Omega - \text{cm}^2$. Previous research, however, indicates that n-contact resistivity in the $10^{-5} - 10^{-6}\ \Omega - \text{cm}^2$ range should be possible [18]. Hence, it indicates that much work needs to be done to fix the current metallization process in order to keep the contact resistance contribution to the overall series resistance low for a large area LPC.

If the contact resistance can be kept small compared to the window/emitter sheet resistance and the finger resistance, however, fabrication efforts can focus on mitigating losses due to the latter forms of resistance. In order to characterize and explore mitigation techniques for the sheet and finger resistance, LPC computer models were developed as described in the following section.

4.2 Computer Modeling

The contact metallization step is but one aspect of the LPC device fabrication process currently in the preliminary stages at AFRL. As is already apparent from just the contact step, relying on extensive fabrication and testing of actual PV cells is a costly and time consuming process. Computer simulations can be used to explore the performance of PV cells under different conditions and can be used in optimizing their structures in order to guide fabrication efforts.

Sentaurus Device is simulation software available from Synopsys, Inc. capable of multidimensional modeling of silicon-based and compound semiconductor devices. It can simulate electrical, thermal, and optical characteristics of semiconductor

technologies by numerically solving coupled systems of equations. The program has numerous device examples including a single-junction GaAs, two-dimensional (2D) PV cell model that can be modified to explore the properties of the program. However, it was not possible to use the 2D GaAs solar cell model to explore the three-dimensional (3D) behavior of current flow, recombination, and resistive losses. Thus, the example was converted into 3D and then further modified into an LPC to compare the simulation results to available experimental results of GaAs LPCs reported by other research groups.

4.3 2D GaAs solar cell example

Generating the Model.

The dimensions of PV devices range from fractions of millimeters for concentrator cells to tens of centimeters for regular solar cells. Modeling the optical and electronic properties of such large devices requires vast amounts of computational power and thus, two-dimensional and three-dimensional models exploit symmetry and periodicity within a device structure to reduce the simulation to the behavior of a unit cell. A unit cell captures all key components of the simulation and can be used to estimate the performance of the entire device. Assuming a parallel grid configuration of metal fingers as was shown in Figure 12b, the device can be reconstructed using multiple unit cells, each of which consists of one quarter of the full finger and one quarter of the total area in between fingers as shown in Figure 18.

This isolation of the unit cell, like the analytic model described in Section 2.6, assumes that the length of the finger is much longer than the finger spacing such that current flows perpendicularly to the finger length. With this assumption, current does not flow directly to the busbar from the semiconductor layers. Thus, in

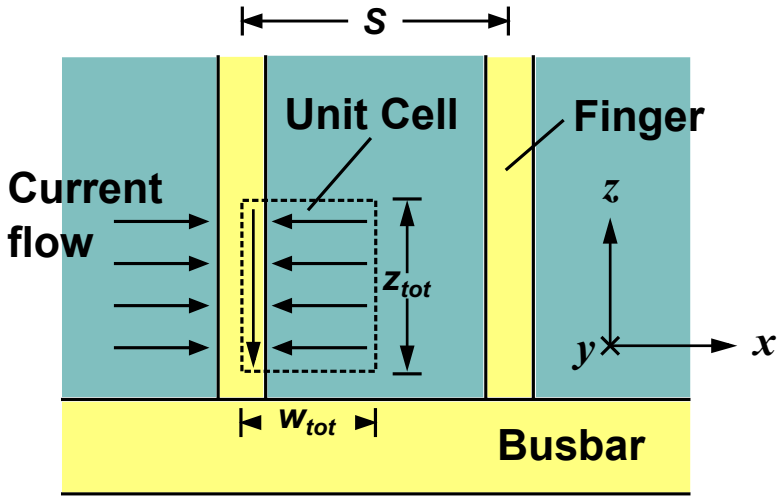

Figure 18. A portion of the parallel grid shown with the unit cell used in modeling the device. w_{tot} and z_{tot} define the total width and length respectively and were varied to investigate the resistance contributions from the semiconductor layers and finger. The dimensions are not to scale in order to show the important features.

3D models, the busbar was not included in the unit cell but rather, current was extracted at the tip of the metal finger where it would attach to the busbar. From Figure 18, it is apparent that a slice of the unit cell parallel to the x-axis would be the same at any position along the z-axis. This uniformity allows for much of the behavior of the solar cell to be captured by a relatively simple simulation of a 2D slice parallel to the xy-plane. The starting point for the desired 3D simulation of a GaAs LPC was a 2D simulation of a single-junction GaAs solar cell provided as an example model available from Synopsys. Table 3 contains the details of the solar cell structure in its unmodified form.

To create the model, the layer boundaries are generated first according to the information in Table 3 defined in a comma separated value file, "sde_epi.csv." The Structure Editor takes the layer information together with any user defined parameters and generates a model of the device. To discuss the dimensions of the

Table 3. Baseline GaAs solar cell structure [20]

Region	Material	Thickness (μm)	Doping (cm^{-3})
cap	GaAs	0.2	n- 1.00e19
window	AlGaAs	0.04	n- 2.00e18
emitter	GaAs	0.8	n- 9.00e17
base	GaAs	3.2	p- 1.00e17
bsf	AlGaAs	0.2	p- 5.00e18
buffer	GaAs	0.35	p- 2.00e18

model without ambiguity, the convention used will refer to the x-dimension as the width, the y-dimension as the thickness, and the z-dimension (in the 3D case) as the length. The width of the unit cell is defined by the parameter w_{tot} (total width) and was originally set to 150 μm. w_{tot} gives half of the finger spacing S of the metal finger grid. The cap layer is then "etched" by deleting all but a portion at the edge defined by the parameter w_{front} (front contact width) which is half of the actual finger width. This was originally set to 5 μm. Thus, 5 μm are left where electrical contact can be made for current extraction. After the etching, an anti-reflection coating is created on top of the exposed window layer consisting of 0.055 μm of TiOx and 0.1 μm of MgF. Finally, the contact windows (lines in the 2D case) are defined where the entire bottom edge of the cell is the cathode and the top of the remaining cap is the anode. The original contacts had zero contact resistance associated with them. The resulting 2D structure is shown in Figure 19.

In order to use the generated model for simulation of carrier generation, recombination, and current flow, etc. it must be divided into a discrete mesh of points that can be used with numerical solvers. The minimum and maximum allowable mesh spacing along different directions and in different regions are specified in the "sde_epi.csv" file. Mesh generation is carried out by Sentaurus Mesh. In generating the mesh, the user defined maximum and minimum spacing are

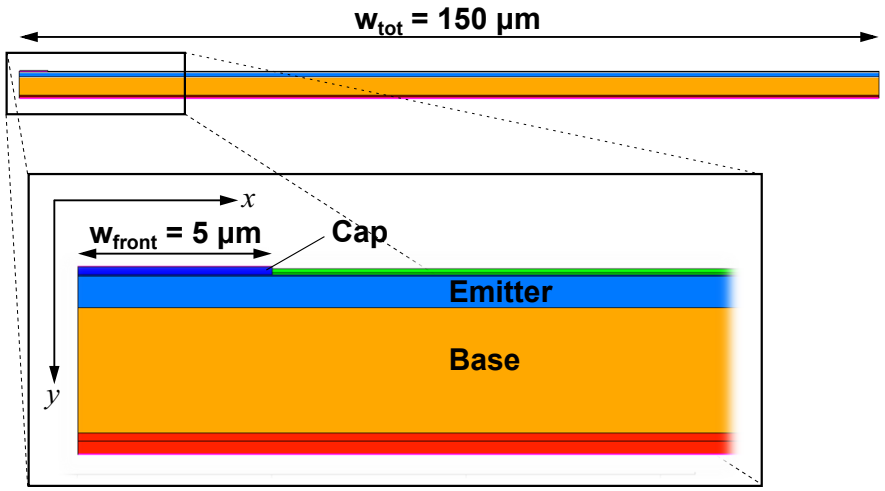

Figure 19. The 2D plane that makes up the GaAs solar cell model. The top of the cap layer is the anode contact which has a width defined by w_{front}, set to 5 μm. The cathode contact is the entire bottom surface (line) of the device with a total width of 150 μm defined by w_{tot} which is half the finger spacing S.

taken into account while trying to maintain a low number of total points that still satisfy the Delaunay condition which generally limits the creation of long, narrow elements of the mesh [21]. The mesh spacing ranges and the Delaunay condition can be broken by the mesh generator to best represent the device which leads to some variability in meshing schemes between models with any coding differences. A close up of the mesh is shown in Figure 20.

The material parameters are defined by the MatPar application using Sentaurus' library of material information as well as parameters in a local parameter file supplied for a specific model.

Simulation.

The simulation of the illuminated cell is carried out by the Sentaurus Device application. The command file for Sentaurus Device contains instructions to determine which physics models and equations might serve the specific research

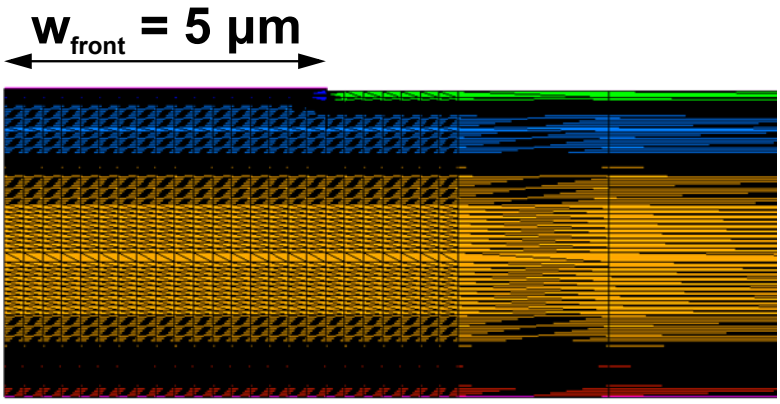

Figure 20. The meshing of the 2D GaAs solar cell. The figure shows the tight meshing spacing under the contact region where there is expected to be high carrier density since the current flows toward the contact. The mesh spacing is more loose beyond the contact region where the carrier density is expected to be lower.

purpose as well as what variables to save as results. It also contains instructions specifying conditions for the simulation including which spectrum to employ, along with the illumination window and angle and polarization of the incident light. The unmodified simulation of the solar cell is illuminated with a spectrum defined in a text file that provides intensity values for discrete wavelengths. The spectrum matches the AM1.5 solar spectrum with total intensity of 100 mW/cm^2 and is plotted in Figure 21. The illumination window spans the top of the device from near the edge of the cap to the end of the device. A slight offset of 10^{-6} μm is added to the edge of the cap before the window starts to prevent illumination of any mesh vertices under the front contact. The light is set to be normally incident with no polarization.

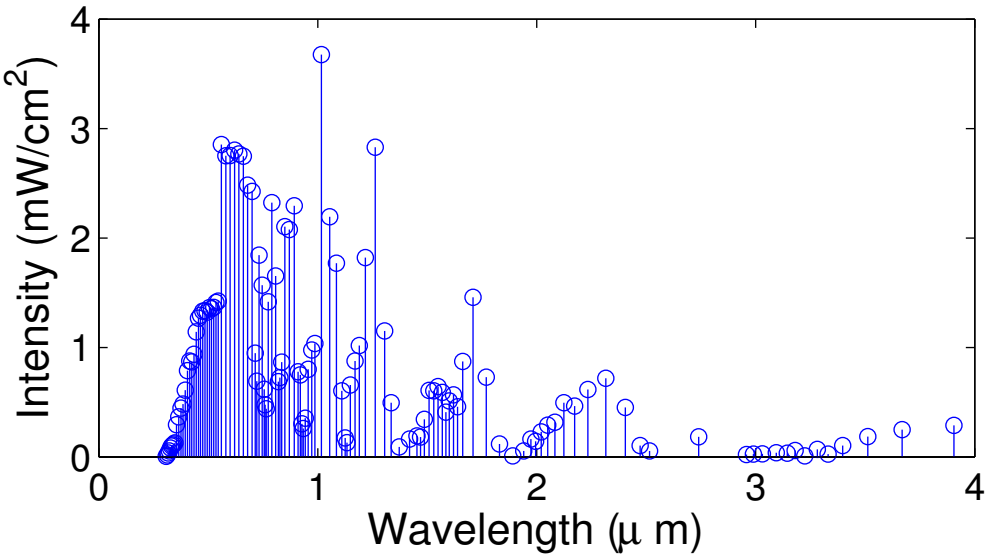

Figure 21. The solar spectrum based on the AM1.5 standard used to simulate the illumination of the GaAs solar cell in 2D and 3D. The optical simulations use discrete wavelengths which can be used individually with different intensities to simulate laser illumination.

Figure 21 is used to highlight the discreet nature of the optical simulation which allows the spectrum to be modified by selecting individual wavelengths such as 810 nm to represent a monochromatic laser source.

In simulating the model under illumination, there are many different dynamic processes that need to be accounted for in combination with one another. The process of optical absorption and carrier generation happen simultaneously with the electrodynamic movement of the charge carriers in the device. To explore the performance of the device, it is important to make the simulation as realistic as possible, a process that involves numerical solutions to sets of differential equations. The equations and the underlying physics models used are explained in the following section and can be found explained in detail in source [22].

Models and Solvers.

The electrostatic potential throughout the device is found by solving Poisson's equation given by

$$\nabla \cdot (\varepsilon \nabla \phi + \vec{P}) = -q(p - n + N_D - N_A) - \rho_{trap} \tag{17}$$

where ε is the electrical permittivity, $\vec{P}$ is the ferroelectric polarization, q is the elementary charge, p and n are the hole and electron densities respectively, N_D and N_A are the ionized donor and acceptor concentrations respectively, and ρ_{trap} represents the trap and fixed charge contributions to the charge density.

The "Physics" section of the Sentaurus Device command file specifies the physical models used in the device and allows customization of the equations used in the simulation.

Fermi statistics are used to calculate the electron and hole concentrations using

$$n = N_C F_{1/2}\left(\frac{E_{F,n} - E_C}{kT}\right) \tag{18}$$

$$p = N_V F_{1/2}\left(\frac{E_V - E_{F,p}}{kT}\right) \tag{19}$$

where N_C and N_V are the effective densities of state given by

$$N_C(m_n, T_n) = 2.5094 \times 10^{19}\left(\frac{m_n}{m_0}\right)^{\frac{3}{2}}\left(\frac{T_n}{300K}\right)^{\frac{3}{2}} cm^{-3} \tag{20}$$

$$N_V(m_p, T_p) = 2.5094 \times 10^{19}\left(\frac{m_p}{m_0}\right)^{\frac{3}{2}}\left(\frac{T_p}{300K}\right)^{\frac{3}{2}} cm^{-3} \tag{21}$$

where $F_{1/2}$ is the Fermi integral of order 1/2, $E_{F,n} = -q\Phi_n$ and $E_{F,p} = -q\Phi_p$ are the quasi-Fermi energies for electrons and holes with the electron and hole quasi-Fermi

potentials of Φ_n and Φ_p respectively. E_C and E_V are the conduction and valence band edges given by

$$E_C = -\chi - q(\phi - \phi_{ref}) \tag{22}$$

$$E_V = -\chi - E_{g,eff} - q(\phi - \phi_{ref}) \tag{23}$$

where χ is the electron affinity, ϕ_{ref} is a constant reference potential given in the case of the GaAs-based device as $\Phi_{intr}(GaAs)$, the intrinsic Fermi level of GaAs. $E_{g,eff}$ is the effective band gap.

The carrier transport model used is the Drift-Diffusion Model. In this model, the electron and hole current densities are given by

$$\vec{J_n} = \mu_n(n\nabla E_C - 1.5nkT\nabla \ln m_n) + D_n(\nabla n - n\nabla \ln \gamma_n) \tag{24}$$

and

$$\vec{J_p} = \mu_p(p\nabla E_C - 1.5pkT\nabla \ln m_p) + D_p(\nabla p - p\nabla \ln \gamma_p) \tag{25}$$

where k is Boltzmann's constant, μ_n and μ_p are the electron and hole mobilities, D_n and D_p are the diffusivites given by $D_n = kT\mu_n$ and $D_p = kT\mu_p$, m_n and m_p are the electron and hole effective masses respectively given by

$$m_n = m_0 \left(\frac{N_C(300 \text{ K})}{2.5094 \times 10^{19} \text{ cm}^{-3}} \right)^{\frac{2}{3}} \tag{26}$$

$$m_p = m_0 \left(\frac{N_V(300 \text{ K})}{2.5094 \times 10^{19} \text{ cm}^{-3}} \right)^{\frac{2}{3}} \tag{27}$$

and $N_C(300K)$ and $N_V(300K)$ are specified for each material in the parameter files. Additionally,

$$\gamma_n = \frac{n}{N_C} \exp\left(-\frac{E_{F,n} - E_C}{kT}\right) \tag{28}$$

and

$$\gamma_p = \frac{p}{N_C} \exp\left(-\frac{E_V - E_{F,p}}{kT}\right) \tag{29}$$

using the aforementioned Fermi statistics for the electron and hole concentrations n and p.

Recombination types are included using the "Recombination (SRH Auger Radiative)" command which covers those types of recombination described in Section 2.2. Trap assisted surface recombination (Section 2.3) is included for the GaAs/GaAs interface as well as the GaAs/AlGaAs interfaces with the command "Recombination (surfaceSRH)."

To include impurity scattering affects on mobility, the command "Mobility(DopingDependence)" is used which allows the mobility to depend on the doping level of each layer. For a GaAs based device, Sentaurus uses the Arora model of doping dependent mobility. The doping dependent mobility is critical in modeling Joule heating (resistive) losses in the device layers as the Joule heat is inversely proportional to the carrier mobility and is given by

$$JH_e = \frac{\lfloor \vec{J}_n \rfloor^2}{qn\mu_n} \tag{30}$$

for electrons and by

$$JH_h = \frac{\lfloor \vec{J}_p \rfloor^2}{qp\mu_p} \tag{31}$$

for holes where $\vec{J}$ is the carrier current density and μ is the mobility.

The optical generation is computed from the spectrum assuming the quantum yield is a step function where the number of carriers generated per photon is one for energies higher than the effective bandgap and zero for photon energies lower than the effective bandgap. This also excludes the possibility of two photon absorption which is expected to be negligible for an LPC. This quantum yield model is specified in the "Optics" subsection of the "Physics" command.

Simulation of the optical processes is carried out using the Transfer Matrix Method (TMM) specified in the "OpticalSolver" command. For all but the thick base layer of the device, the intensity pattern is given as a standing wave where the intensity of the light is calculated by

$$I = Re(A + B)^2 + Im(A + B)^2 \tag{32}$$

where A and B are the forward and backward-propagating wave complex field amplitudes. For the base layer, an "Envelope" intensity pattern is used where the intensity of light is given by

$$I = Re(A)^2 + Im(A)^2 + Re(B)^2 + Im(B)^2 \tag{33}$$

to reduce interpolation errors resulting from non-resolved standing wave patterns [20].

By default in Sentaurus, the surrounding medium of a model is vacuum. The substrates on which the device layers would be grown are typically available on the order of several hundred microns [17]. Since the substrate thickness is much longer than the incident wavelength of light, the optical properties can be realistically simulated by assuming an infinitely thick substrate layer, using the command

"LayerStackExtraction" to specify an infinite GaAs substrate on the bottom of the device.

The illumination window size and location, along with the polarization and incidence angle of the simulated light are specified with the "Excitation" command.

The "Math" section of the Sentaurus Device command file controls the type of solver for the coupled differential equations [17, 24, 25]. The solver used in the simulation is the blocked decomposition method.

The "Solve" section of the Sentaurus Device file sets up the voltage ramp that is used to generate an IV curve. First, a quick ramp is done using large voltage steps where only the general trend of the IV curve is needed from $V = 0$ V to $V = 7$ V variable depending on the expected location of the voltage at the maximum power point (V_{mpp}). Then, a slow ramp using small voltage steps is completed from the end of the first ramp through the open circuit voltage. A capture of all of the data requested in the "Plot" section is completed at a voltage of 0.9 V near the expected V_{mpp}. The data includes current densities, electric potential, optical generation and recombination rates.

Default units for the extracted current I' from any 2D device in Sentaurus Device are A/μm. This assumes that the length of the device in the z-direction is 1 μm. By computing the current in these units, rather than in A, the results can be multiplied by the actual device length to predict the total current. Since the 2D unit cell of the solar cell is also truncated in the x-direction, the units need to be computed in current per unit area which is given as current density J. To convert A/μm to mA/cm^2 the current is multiplied by an "area factor." The area factor is given by the extracted current I' divided by the length of the device in the x-direction in μm which is specified by the parameter w_{tot}. The area factor also contains the conversion from A/μm^2 to mA/cm^2 which is 10^{11}. Thus the area factor

in the 2D model is $10^{11}/w_{tot}$. Running the simulation without any modifications predicts an efficiency of 22.78%, and a FF of 85.49%.

4.4 2D to 3D solar cell

To ensure changes made in converting the 2D device to 3D did not invalidate the model, the device was extended into the z-direction while attempting to maintain the same simulation results. Thus, the code was modified with only those changes necessary to create a 3D structure under the same illumination conditions. First, a new parameter was created in the Structure Editor command file to define the length of the device z_{tot} (total length in z-direction) in μm. Then, the contact windows were redefined from lines to full rectangles that span the length of the device to ensure the full surface of the cap was covered for the anode contact and the full bottom surface was covered for the cathode contact. Then, the illumination window was similarly changed from a line to rectangle covering the absorbing portion of the cell (the top surface excluding the cap) in the Sentaurus Device command file. In order to prevent optical generation beneath the contact, the illumination window was offset from the edge of the cap layer by 10^{-6} μm as it was in the original 2D simulation. All of the dimensions necessary to define the aforementioned contact and illumination windows depend only on the parameters w_{tot}, w_{front}, and z_{tot} so they change along with the unit cell dimensions.

In the 2D model, the extracted current I' in units of A/μm was converted to a current density J in units of mA/cm^2 by multiplying by an area factor of $10^{11}/w_{tot}$. In the 3D model, the area factor had to include the actual length of the device in the z-direction (rather than the default of 1 μm). Accordingly, the area factor was adjusted to $10^{11}/(w_{tot} \times z_{tot})$.

The 3D meshing scheme required the most amount of adjustment. The total number of points in the 2D mesh remains relatively low for even very small mesh spacing in the y-direction. Without changing any of the mesh dimensions for the 2D plane while extending it into the z-direction with mesh spacing given by dz would roughly result in z_{tot}/dz times the original number of points. This means that any simplifications to the mesh (increasing the spacing) in the y-direction would greatly reduce the total number of points and thus reduce the model generation and simulation run times. Thus, the mesh spacing was broadened in the largest layers as can be seen in Figure 22. Figure 22 shows the 3D device.

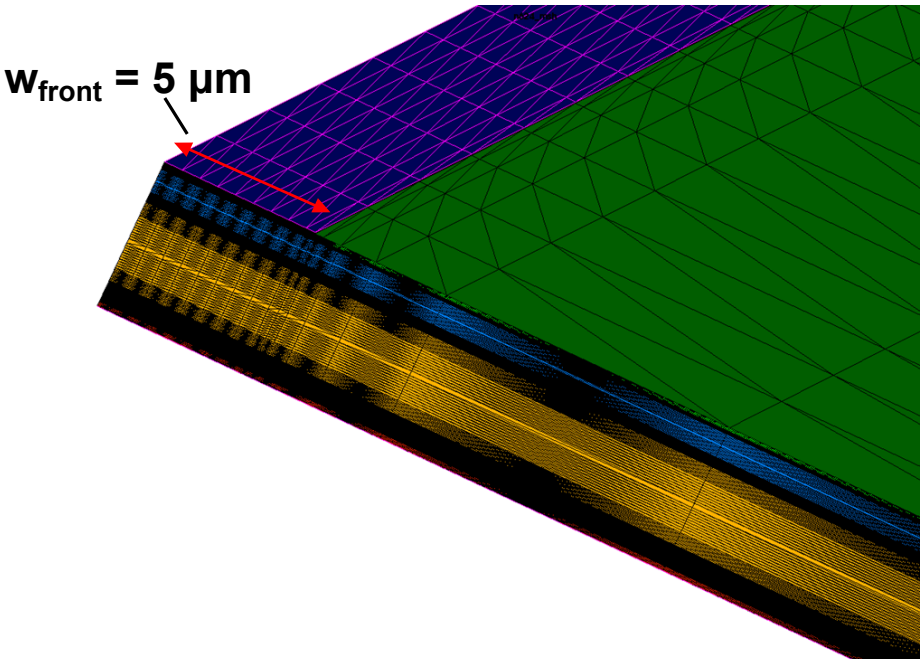

Figure 22. The meshing of the 3D GaAs solar cell. The y-directional mesh spacing is loosened from the 2D unit cell shown in figure 20 in order to reduce the total number of points when the device is extended into 3D.

The results of the 3D solar cell were compared to the 2D solar cell to ensure the 3D model development was done correctly and produced consistent results. The IV curves for the 2D solar cell and a 1 cm long 3D solar cell are both given in Figure 23 where the key performance parameters are compared in Table 4 showing consistency in the simulation results.

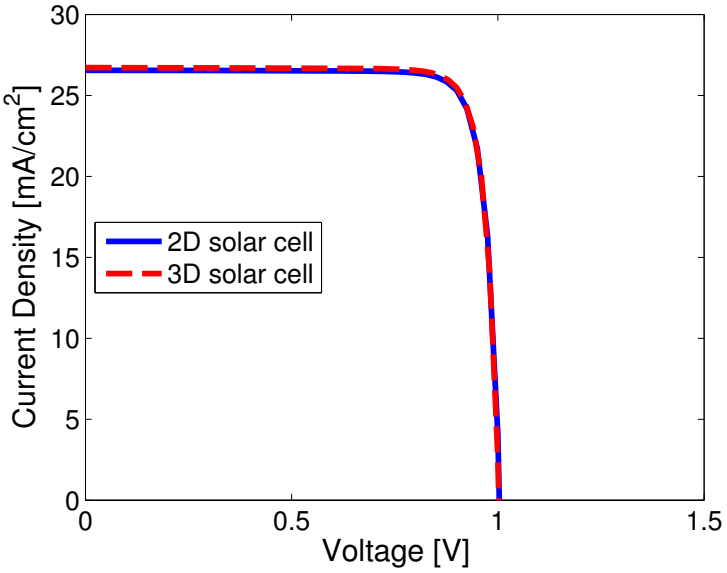

Figure 23. Comparison of the IV curves of the 2D and 3D (1 cm long) GaAs solar cell models under AM1.5 illumination. The curves shows good agreement through the entire voltage range and verify that the 3D meshing scheme was appropriate.

Table 4. 2D and 3D GaAs solar cell performance

Model	J_{sc}(mA/cm^2)	$V_{oc}(V)$	$FF(\%)$	$Eff(\%)$
2D	26.55	1.004	85.49	22.78
3D	26.72	1.002	85.46	22.93

In changing the model from 2D to 3D, the computation time required to generate the models and simulate the IV characteristics increased significantly. The 2D simulations took a matter of minutes using a computer with a dual-core processor. The 3D simulations took up to several hours for each model with different parameters using a computer with 16 processors running in parallel.

4.5 Solar Cell to Laser Power Converter

After confirming the operating 3D model of the solar cell, the model was modified in order to examine the performance of an LPC with gold grid metal fingers. Traditional solar cells contain a metal finger grid used for current extraction on top of the cell. To investigate the contribution of the metal resistance to the overall series resistance of the cell, a gold finger was placed on top of the cap layer with a cross section of originally 5 μm wide by 5 μm in height. A new parameter *dGold* was created to make the finger dimensions variable (w_{front} already defined its width). The anode contact window was redefined to cover only the end tip of the gold finger. This end tip in a real device would connect to a continuation of the finger and eventually terminate at a bus bar as seen in the unit cell in Figure 18. This is a key modification as it forces all of the current to flow through the finger rather than being extracted when it reaches the edge of the unit cell as in the 2D solar cell model. Losses due to contact resistivity of the contacts were not modeled in order to isolate the resistance contributions from the bulk semiconductor layers and grid metal fingers. Gold has a resistivity of $2.26 \times 10^{-6}\ \Omega - \text{cm}$ at 300 K which was parameterized with a new parameter *ResGold* to explore the effect of different values on the LPC performance.

The AFRL LPC will be illuminated by a monochromatic source operating at 1550 nm with the structure tailored for conversion of the 1550 nm source. GaAs,

which makes up the base and emitter layer of the solar cell model, has a bandgap of 1.4225 eV at room temperature. Photons with a comparable energy would have a wavelength of 870 nm. Using a laser source with a slightly higher energy photons ensures nearly all of the photons are absorbed. This has lead several groups experimentally investigating GaAs LPCs to use a 810 nm laser source. To be able to better compare the simulated results with experimental results available in the literature, the spectrum file was modified to consist of only one wavelength at 810 nm with an illumination intensity of 10 W/cm^2.

The original 2D example was created with an anti-reflection coating designed to reduce reflection over the whole solar spectrum using MgF and TiOx. Since the illumination source was changed to a monochromatic source at 810 nm, the anti-reflection coating could be optimized for this specific wavelength. The window layer is the topmost layer of the device and consists of $Al_{0.8}Ga_{0.2}As$. To minimize reflection at a wavelength of 810nm, a 101 nm thick layer of Si_3N_4 was used with a predicted reflectance of 1.596% [23].

4.6 Fraunhofer Institute-based LPC

As mentioned in Section 3.2, comparing simulation results to experimental results can help identify the strengths and weaknesses of a simulation. There were no experimental results to compare or verify the results of the GaAs solar cell or the 810 nm LPC but there are, however, a number of other LPC designs that have recorded experimental results in the literature. One design, created by the Fraunhofer Institute and discussed in Section 3.2, was similarly based on GaAs but contained differences to the layer structure such as the placement of a highly doped lateral conduction layer (LCL) on the top surface [9].

The information provided in the investigation of the cell included the layer materials and type of doping but did not reveal the layer thicknesses or the exact doping amounts as shown in Table 1. The layer thickness of the LCL was 400 nm. Based on this information and the existing GaAs LPC device model already created, a new cell was designed that allowed comparison to the experimental results of the Fraunhofer Institute design. The exact layer structure is given in Table 5 below.

Table 5. Model based on Fraunhofer Institute LPC in Table 1

Region	Material	Thickness μm	Doping cm^{-3}
cap	GaAs	0.2	n- 1.5e19
LCL	GaInP	0.4	n- 8.0e18
window	GaInP	0.2	n- 5.0e19
emitter	GaAs	0.8	n- 9.00e17
base	GaAs	2.8	p- 1.00e17
bsf	GaInP	0.2	p- 5.00e18
buffer	GaAs	0.35	p- 2.00e17

In developing the Fraunhofer Institute based LPC (FLPC) it is important to note that heavy doping can become a problem due to increased free carrier absorption as discussed by Bett [9]. Thus, the LCL was kept relatively thin at 400 nm and doping was kept below 10^{19} cm^{-3}. The window doping, however, was changed to 10^{19} cm^{-3} in order to match the Fraunhofer design. The effect of the high doping on GaInP absorption and index of refraction is unknown and may need to be considered in future work by providing additional material parameter files to Sentaurus.

The device that the above layer structure is based on was tested at the Fraunhofer Institute with an 810 nm laser source with non-uniform illumination and achieved an efficiency of approximately 52.5% at a power density of 10 W/cm^2 [9]. The 2D FLPC model achieved a peak efficiency of 58.92% at a finger spacing of

240 μm, dropping to an efficiency of 52.68% at a finger spacing of 780 μm. As expected, the efficiency of the 2D model outperformed the experimental results for several reasons. The uniform illumination of the model prevents parasitic current compared to the non-uniform illumination used in the experiment. The ideal infinite shunt resistance in the model also prevents leakage current. In addition, the 3D series resistance contributions were not yet accounted for and were expected to lower the efficiency further. Thus, taking into consideration the above difference between the simulation and experiment, the comparison of the results serves as evidence that the simulation produced reasonable and expected results. Further manipulation of the 3D FLPC showed efficiencies between 50% and 60% discussed in the following results chapter.

4.7 Relating Finger Length to Cell Area

The 3D unit cell used in the simulation allows for the efficiency to be explored as a function of finger dimensions as well as finger spacing. Often, when efficiencies are reported for experimental results, the area of the PV cell is given. Thus, relating the unit cell to the area is necessary to compare simulated and experimental results. When converting from unit cell length to PV cell area, some key assumptions are made. The first assumption is that current does not flow directly to the busbar. If this were the case, the busbar would need to be included in the unit cell. This is a reasonable assumption where the finger lengths are long that most of the area of the device is much closer to a nearby finger than the surrounding busbar.

For the parallel grid shown in Figure 12b, it is a simple conversion. The area of a square parallel grid is $(2 \times z_{tot})^2$. For the inverted square grid shown in Figure 12a, estimating efficiency versus area based on the simulated unit cell is more involved.

First, it is assumed that current generated anywhere in the cell flows to the nearest finger. Thus, each finger has an area from which it collects current as shown in Figure 24. From the Figure, it is apparent that there are three types of fingers. Type I fingers are the four that intersect in the center. There are eight Type II fingers which cover the corners of the grid. Type III fingers are those in between. The number of type III fingers in between the type I and type II is given by $N_{III} = L_{mf}/S - 2$ where L_{mf} is the maximum finger length (the length of those intersecting in the center) and S is the finger spacing. These are the type I fingers but the subscript I will be reserved for the effective length of these fingers. The total number of type III fingers is then $8N_{III}$.

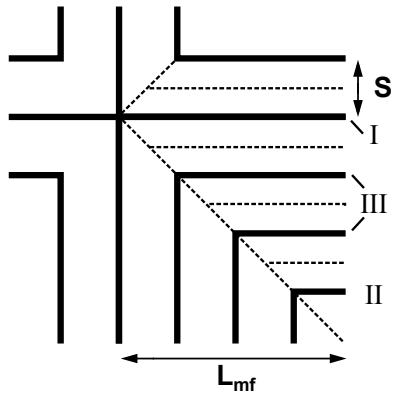

Figure 24. A portion of the inverse square grid where the maximum finger length L_{mf} is four times the finger spacing S and there are thus two type III fingers. Each finger collects current from the enclosed dashed area around them given by Equations 34, 35 and 36.

The areas of responsibility for the different types of fingers are given geometrically by

$$A_I = L_{mf}S - (S/2)^2 \tag{34}$$

$$A_{II} = (9S^2/8) \tag{35}$$

$$A_{III}(n) = (L_{mf} - nS)S, n = 0, 1, 2, ..., N_{III} \tag{36}$$

The simulation results provide efficiency values for a unit cell of an LPC and can be interpolated to give a function $Eff = f(L)$. The second assumption is that the effective finger lengths of the different types of the fingers is given by their area of responsibility divided by the finger spacing. Thus the effective finger lengths are given by

$$L_I = L_{mf} - S/4 \tag{37}$$

$$L_{II} = 9S/8 \tag{38}$$

$$L_{III}(n) = L_{mf} - nS, n = 0, 1, 2, ..., N_{III} \tag{39}$$

Now, the total efficiency of the inverted square grid Eff_{IS} can be estimated by summing the efficiencies of the individual unit cells weighted by their area of responsibility and dividing by the total area, A_T given by $A_T = (2L_{mf})^2$.

$$Eff_{IS} = \frac{4A_I f(L_I) + 8A_{II} f(L_{II}) + 8\sum_{n=0}^{N} A_{III}(n) f(L_{III}(n))}{A_T} \tag{40}$$

Equation 40 provides an approximation of the efficiency of the inverse square grid by geometrically relating the simulation unit cell to the inverse square grid in order to provide insight into how the resistive losses explored affect the ability to scale the area of a high power PV device. The following chapter describes how the Original Laser Power Converter (OLPC) and the FLPC models were adapted to characterize the resistive losses and the results of the investigation.

V. Results

The original laser power converter (OLPC) given by Table 3 and the Fraunhofer laser power converter (FLPC) given by Table 5 were used to investigate the sources of resistive losses. Earlier results on high power solar photovoltaics [15] [16][17][18] indicate that the two main sources of series resistance loses are in the metal fingers and the top window/emitter layer. In order to estimate the power loses and relative importance of each effect, a series of four different simulation investigations were undertaken.

The first section describes how the 2D models were used to find the affect of the finger spacing on the efficiency of the models which is related to the losses in the window/emitter layers. The second section describes how the resistivity of the gold grid metal fingers in the 3D model was altered to see if the finger losses would be appreciable at short finger lengths. The third section describes how models with different grid metal resistivities and thicknesses were lengthened in the dimension parallel to the finger to compare the results with the CPV research discussed in Section 3.2 and to determine how the cross-sectional area of the grid metal fingers in an LPC could be increased to mitigate the resistive loss associated with increasing the finger length.

5.1 2D Efficiency vs Finger Spacing

In order to isolate the resistive losses that result from current flowing laterally in the window/emitter layers to the contact finger, a set of two dimensional models were created with varying finger spacings (different values for the parameter w_{tot}). The 2D models used in the simulations did not have a gold region on top of the contact cap so no additional losses in the finger were included. The contact window

(line) was directly on top of the contact cap layer. Figure 25 shows the efficiency as a function of finger spacing generated by this simulation for both the OLPC and the FLPC under the same illumination conditions of a 10 W/cm^2, 810 nm source.

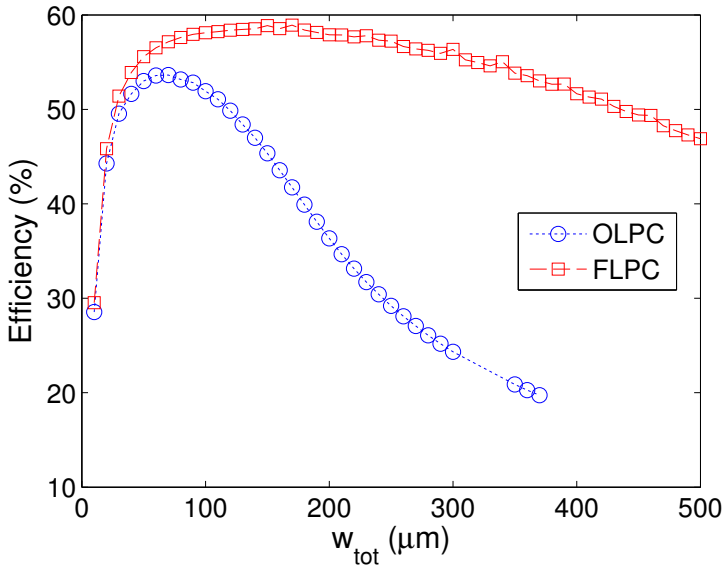

Figure 25. Figure shows the efficiency of the 2D OLPC and FLPC models as they were lengthened in the x-direction, equivalent to increasing the finger spacing. The decrease in efficiency while increasing the finger spacing is less pronounced for the FLPC with an LCL, indicating less resistive loss in the lateral current flow that would otherwise be in the emitter and window layers.

Figure 25 shows that even small increases in the finger spacing significantly impact the efficiency of the device. There is a significant difference, however, in the effect that increasing the finger spacing has on the two designs. Both showed an initial increase in efficiency as the finger spacing increased up to a maximum value beyond which the efficiency decreased. The shape of the curves beyond their maximum efficiency values differ greatly between the OLPC and FLPC. The OLPC curve shows a much more rapid decline in efficiency before the losses begin to taper at an inflection point near $w_{tot} = 180$ μm.

At low values of w_{tot}, the OLPC and FLPC efficiency curves are very similar due to the dominance of shadowing losses which are more pronounced at smaller finger spacings as discussed in Section 2.7. The width of the front contact in both simulation sets was given by $w_{front} = 5$ μm which corresponds to a physical contact width of 10 μm. The shadowing factor was calculated by $(w_{tot} - w_{front})/w_{tot}$ yielding a value of 50% for $w_{tot} = 10$ μm. The same parameters used in the 2D simulations were used to generate the shadowing loss example plot in Figure 11. Since the goal of the simulation was to investigate resistive losses in the lateral flow of current as a function of finger spacing, the shadowing losses were factored out of the efficiency calculations by dividing by the shadowing factor.

When the shadowing losses were not included, the efficiency drop for small finger spacings nearly disappeared while the general shapes of the two curves presented in Figure 25 stayed the same for larger finger spacings. The new efficiency curves are shown in Figure 26.

The drop in efficiency $\Delta\eta$ can be found by subtracting the minimum efficiency from the peak value. In order to find the change in efficiency normalized to the peak value $\Delta\eta_{norm}$, the difference must be divided by the peak value and multiplied by 100. This procedure is given by

$$\Delta\eta_{norm} = 100 \times \frac{\eta_{max} - \eta_{min}}{\eta_{max}} \tag{41}$$

where η_{max} and η_{min} are the peak and minimum efficiencies respectively.

The 2D OLPC simulations results showed $\Delta\eta$ of 39.43% and $\Delta\eta_{norm}$ of 66.34% when w_{tot} was increased to 370 μm whereas the 2D FLPC results only showed a $\Delta\eta$ of 14.38% and a $\Delta\eta_{norm}$ of 23.29% when w_{tot} was increased to 500 μm.

Excluding shadowing losses shifted the optimum finger spacing for the two designs to much lower finger spacings. More importantly, it allowed the resistive

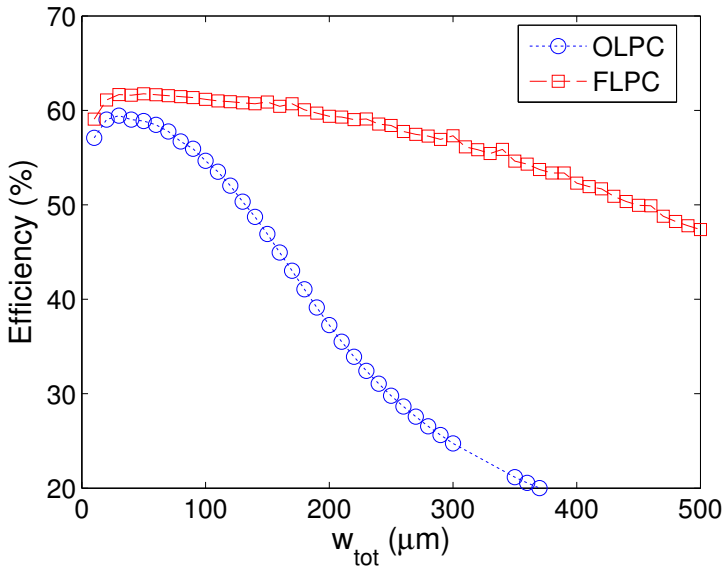

Figure 26. Figure shows the simulations under the same conditions as Figure 25 but removes the shadowing loss by dividing by the shadowing factor, $(w_{tot} - w_{front})/w_{tot}$, so that the efficiency drop is due primarily to the increased resistive loss from the lateral flow of current. This results in higher efficiencies for smaller finger spacings and shifts the maximum efficiency to lower finger spacings.

losses to be isolated in order to compare them with the predicted losses given by the analytic model discussed in Section 2.6.

In the 2D case for which there were no finger losses, the total resistive losses are given by Equation 10 according to the analytic model. Calculating the analytic losses requires the sheet resistivity of the window/emitter layer ρ_e, the finger spacing S and the extracted current density J. J is calculated in the simulations in units of mA/cm^2 and S is a known parameter given by $2 \times w_{tot}$. The remaining unknown, ρ_e, is dependent on the mobility of the semiconductor layers and the carrier concentrations and is variable throughout the device.

In order to find the effective sheet resistance based on the analytic model where the I^2R losses are given in by Equation 10, the losses were calculated from the efficiency data. First, the efficiencies without shadowing loss were calculated by

dividing by the shadowing factor. Additional sources of loss were eliminated by subtracting all the efficiency values from the peak efficiency. The analytically predicted losses were divided by the incident power of 10 W/cm^2 to compare loss percentages. Equation 10 was then fit to the losses with the unknown parameter ρ_{sh} in place of ρ_e. The effective sheet resistances were found to be 1337.96 Ω/□ and 105.92 Ω/□ for the OLPC and the FLPC respectively. Figures 27 and 28 show the analytic and simulated losses for the OLPC and FLPC respectively.

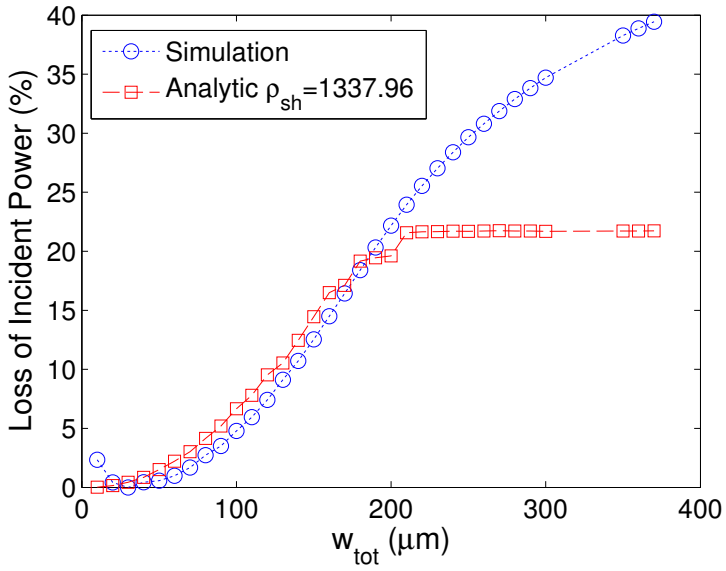

Figure 27. Analytic fit to the window/emitter losses for the OLPC resulting in an effective sheet resistance of 1337.96 Ω/□ for the portion before the analytic model levelled off. The knee in the analytic prediction is due to the current dropping in the device as shown in Figure 29 which dropped the efficiency of the device but also decreases the predicted resistive losses. The fitted portion had an R^2 value of 0.958.

The effective sheet resistivity calculated for the FLPC was much less than that of the OLPC which is largely attributed to the LCL on the former. Previous work on GaAs concentrator cells have used a value of 300 Ω/□ for the emitter sheet resistivity with a doping of 2.5×10^{18} cm^{-3} [24]. The FLPC value was expectedly

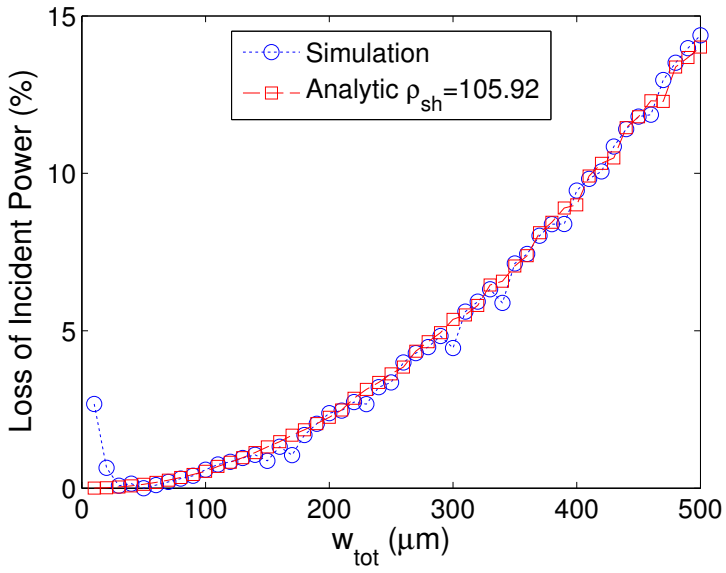

Figure 28. Analytic fit to the window/emitter losses for the FLPC resulting in an effective sheet resistances of 105.92 Ω/□**. The fit resulted in** $R^2 = 0.988$**.**

lower, likely due to the highly doped LCL while the OLPC value was significantly higher. This may have been due to lower doping and thinner layer thicknesses of the OLPC. Figure 28 shows excellent agreement between the analytic and simulated results. Figure 27, shows that the losses predicted by the analytic model level off near $w_{tot} = 210$ μm as the current output of the device begins to drop off for larger values of w_{tot} for the OLPC. The simulated currents for the OLPC were plotted as a function of w_{tot} in Figure 29 to illustrate the current drop. The drop was not present in the FLPC as shown by Figure 30 which explains why the analytic model maintained good agreement throughout the range of w_{tot} used. This indicates that in addition to causing resistive heating losses, resistance throughout the device can reduce efficiency by lowering the output current.

In addition to the efficiency of the models with different finger spacings, the FF of the IV curves provide an indication of increased series resistance. The two diode model discussed in Section 2.1 uses Equation 4 to model the IV characteristics of a

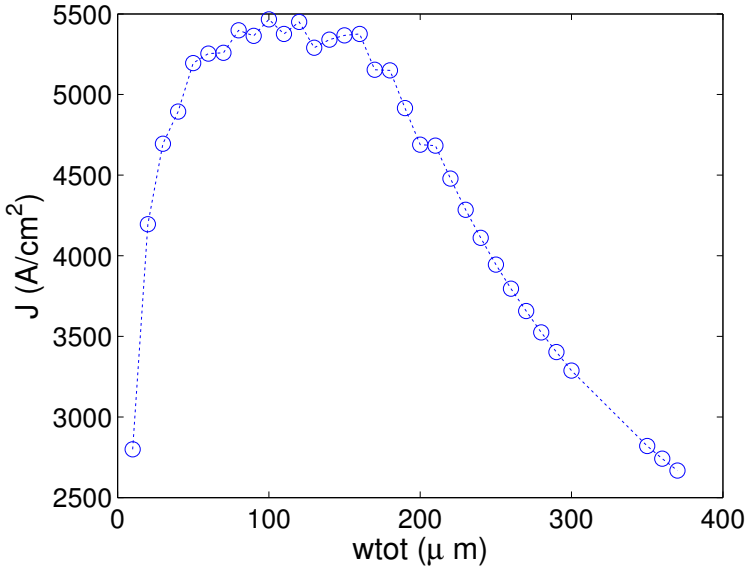

Figure 29. Output current density of the 2D OLPC vs w_{tot}. The figure shows that at large finger spacings, the current was reduced which lead to a drop in efficiency that was not predicted by the analytic loss model.

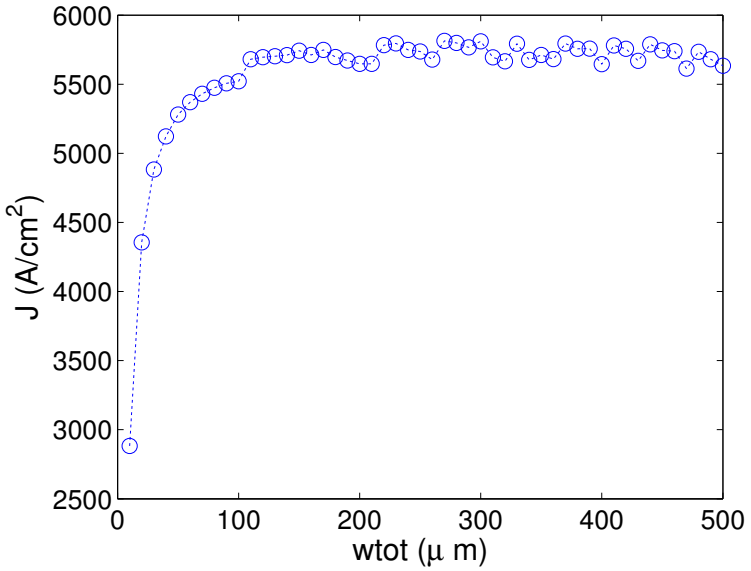

Figure 30. Output current density of the 2D FLPC vs w_{tot}. The figure shows that the current levelled off at high values of w_{wot} but did not drop as it did for the OLPC.

PV cell. The series resistance appears in three places in Equation 4. It affects the IV characteristics of both of the diodes and reduces the overall current in the final term as a series resistor in conjunction with the parallel shunt resistance. Since the models are completely isolated in space with no possibility of leakage current, the shunt resistance is assumed to be infinite such that any shift in the IV curve is due to the series resistance. From the two diode model, it is apparent that increasing the finger spacing not only increases I^2R losses but also affects I itself, the extent of which can be captured by the FF. Figure 31 shows the FF as a function of w_{tot} for both of OLPC and the FLPC.

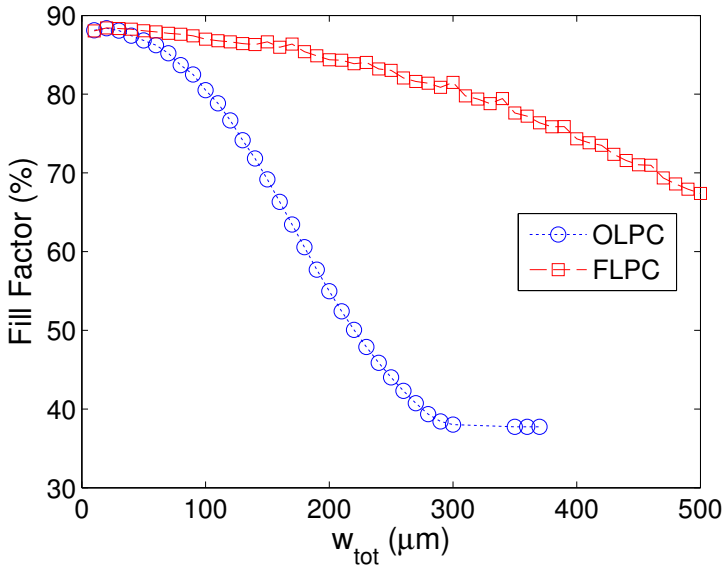

Figure 31. Figure shows the fill factor plotted as the two-dimensional simulation was lengthened in the x-direction, equivalent to increasing the spacing between fingers. Results from both the OLPC and FLPC models are shown. The decrease in fill factor with increasing finger spacing is less pronounced for the FLPC with an LCL, indicating lower total series resistance.

The figure shows that both designs start out with high fill factors at low finger spacing values. As the finger spacing increases, the FF decreases. However, for the

FLPC with the LCL, the FF drops much more slowly due to the difference in total series resistance.

Although the FLPC is not the same layer structure as the original, the primary differences are higher doping and larger thicknesses of the window and added LCL layers. These changes, the results suggest, can help maintain the FF and the efficiency while extending the finger spacing. The following sections discuss the exploration of the three dimensional devices which show large grid metal fingers may work in tandem with the LCL in enabling the models to be extended along the length of the finger while maintaining high efficiency.

5.2 3D Efficiency vs Gold Resistivity

In order to increase the area of an LPC, the two fundamental methods are increasing the finger spacing and increasing the finger length. The previous section detailed the exploration of different finger spacings using a 2D model but in order to characterize the finger losses, a 3D model is necessary. It is worth noting that almost amp levels of current need to be extracted from metal finger contacts with an approximately 25 μm^2 cross sectional area. Hence, significant finger resistive losses are anticipated at high power levels.

The analytic model for the resistive losses in the finger given by Equation 13 indicates that the losses have a linear dependence on the bulk resistivity of the grid metal ρ_F such that for higher resistivity values, the affect of altering the other variables such as H_f,W_f and L_F should be more pronounced. Previous work on concentrator solar cells has shown that depending on contamination of the grid metal and the processing steps used, the metal resistivity can increase up to $6-8$ times the pure metal value [19]. Thus, a new parameter was created in the model to explore how the gold resistivity affected the efficiency and losses in the device. It

was soon realized that this gold resistivity factor could serve a second but even more vital purpose. During preliminary 3D calculations for long fingers, the simulations failed to converge for fingers longer than 6000 μm. By increasing the gold resistivity to an artificially high value, it is possible to effectively simulate very long finger lengths with only modest computation resources. By investigating smaller devices with increased finger resistivity, the expected trends for longer devices were explored. The new parameter,the GRF was multiplied by the resistivity of gold. The other parameters were fixed with $w_{tot} = 150$ μm, $z_{tot} = 300$ μm, $w_{front} = 3$ μm, and the finger height $H_f = 0.5$ μm. Because of the quadratic dependence of the finger losses on the finger length, a GRF of 100 and a simulated finger length of 300 μm relates to an effective finger length of 3 mm. It is these kind of finger lengths that are required to make an LPC cell with areas on the order of 6 cm^2. Because of the interaction between the lateral conduction layer and the metal fingers, this GRF-based technique was not expected to accurately predict the efficiency of longer cells. However, it was useful to show the expected efficiency trends as the finger length was increased before investing time in longer cells requiring much more computation time. As used previously as an example, Figure 6 in Section 2.1 gives the IV curves for the OLPC with different GRF values. Figure 32 shows how the efficiency dropped for both the OLPC and FLPC with increasing GRF.

Figure 32 shows that the OLPC dropped from a peak efficiency of 46.19% at a GRF of 1 to an efficiency of 31.17% at a GRF of 100. In order to see the influence of the grid metal resistance, the 3D results were compared to the 2D efficiencies by setting η_{max} in Equation 41 to the efficiency simulated at $w_{tot} = 150$ μm for the respective 2D OLPC and FLPC models. The performance changes as the GRF was increased to 100 compared to the the 2D simulations are shown in Table 6.

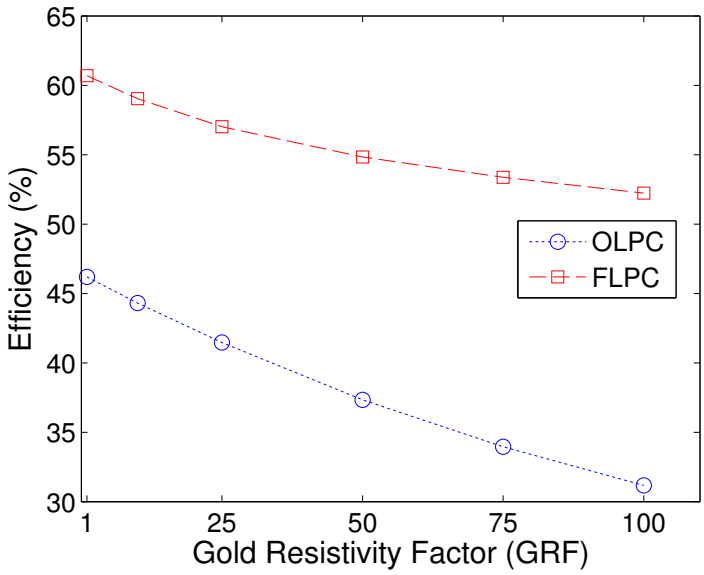

Figure 32. Comparison of the efficiencies of the two LPCs as the resistivity of the gold fingers was multiplied by a factor (GRF) increasing from 1 to 100. The FLPC dropped only 8.46% compared to the OLPC which dropped 15.02% when the GRF changed from 1 to 100.

Table 6. LPC performances with $z_{tot} = 300$ μm and GRF reaching 100

model	$\Delta\eta(\%)$	$\Delta\eta_{norm}(\%)$	$\Delta FF(\%)$
OLPC	15.12	32.20	21.65
FLPC	7.59	12.47	11.86

Table 6 shows that FLPC showed a smaller drop in efficiency and FF than the OLPC as the GRF was increased. This result suggests that the LCL on the FLPC helped mitigate the losses as the resistivity of the metal fingers increased. A comparison with the analytic model was used to explain why that might be the case.

The predicted losses based on the analytic model given by Equation 13 were found and plotted along with the scaled losses determined from the simulated efficiencies. The shadowing losses were removed as they were in the previous section and then the efficiencies were subtracted from the efficiencies (without shadowing) of the 2D models found at $w_{tot} = 150$ μm. Removing the shadowing losses is critical in comparing devices with different front contact widths. Without shadowing, the

efficiency results of the 2D simulations were expected to be higher than the peak efficiency of the 3D device at a GRF of 1. After scaling the efficiencies based on the 2D results, the loss percentages were multiplied by the incident power of 10 W/cm^2. Unlike the analytic model of window/emitter losses given by Equation 10 with an unknown sheet resistance, all of the parameters of Equation 13 are known. Figures 33 and 34 compare the analytic and simulated losses for the OLPC and FLPC respectively.

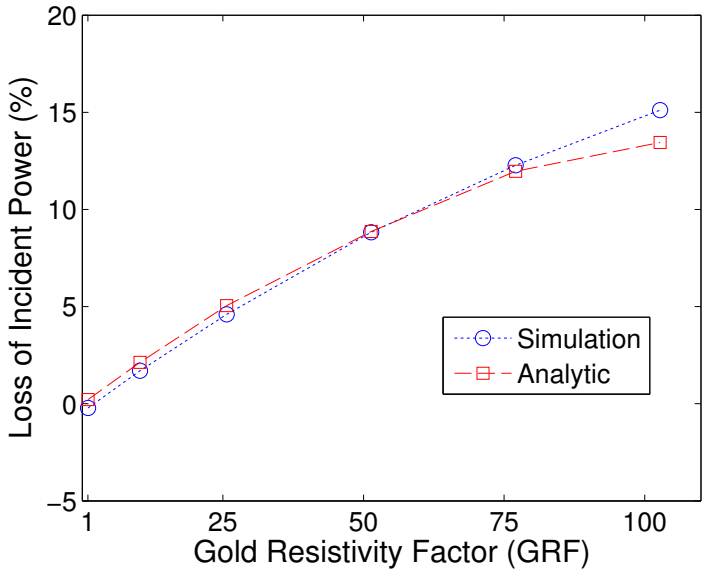

Figure 33. Comparison of the analytic and simulated finger losses for the OLPC for a 300 μm **device with varying GRF. Comparison of the curves resulted in** $R^2 = 0.981$**. The curves begin to diverge as the current shifts from perpendicular to the finger as shown in Figure 35.**

The slight negative losses shown for a GRF of 1 in Figures 33 and 34 are due to the 3D simulations performing slightly better than the equivalent 2D simulations since the simulated finger losses are found by using the 2D simulated efficiency as a baseline. These results provide an indication of the error in the simulations which

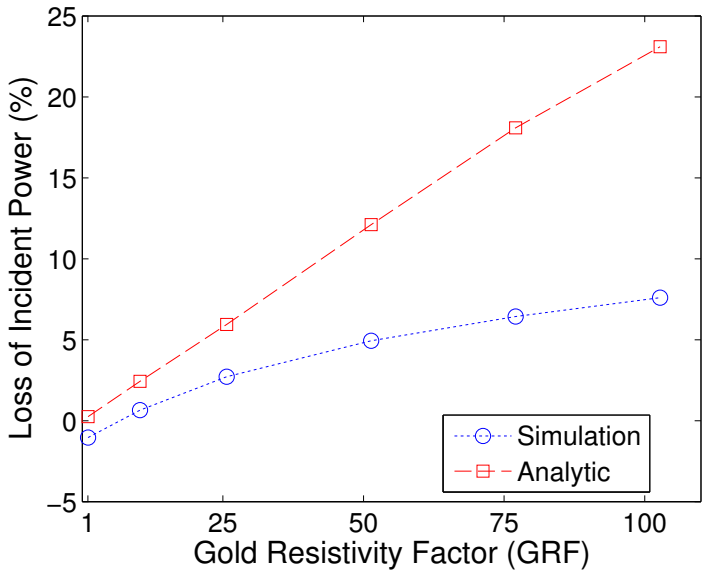

Figure 34. Comparison of the analytic and simulated finger losses for the FLPC for a 300 μm device with varying GRF. Comparison of the curves resulted in $R^2 = -6.81$ since they did not overlap. The curves are significantly different in shape due to the current no longer flowing perpendicular to the finger as assumed in the analytic model and shown in Figure 36.

was also apparent by the small differences between the 2D and 3D solar cell model results given in Table 4.

Figure 33 shows close agreement between the simulated and analytic losses for the OLPC whereas Figure 34 shows that the analytic model predicts significantly larger power losses than were seen in the FLPC simulation. To see why there was such large disagreement between the simulated and analytic models for the FLPC, current density streamline plots were created for the OLPC and FLPC models with different GRFs. Figures 35 and 36 show the device models from a top down perspective in which the device layers were made transparent in order to reveal the current streamlines. For the OLPC, the current flows nearly perpendicular to the finger for all GRF values in line with the assumptions that went into the analytic

model development. For the FLPC, however, the current began traveling toward the contact tip of the finger at higher GRF values.

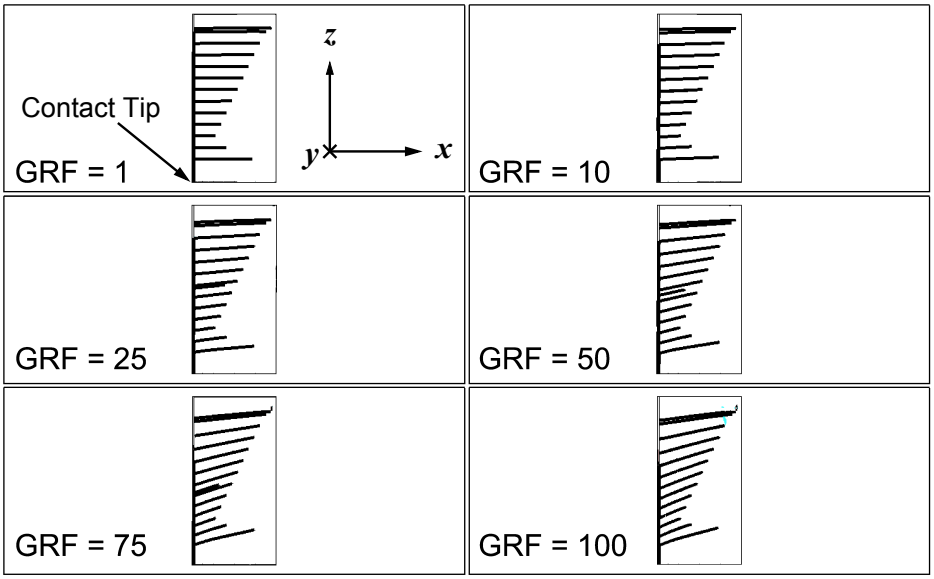

Figure 35. Current streamline plots for the OLPC with $z_{tot} = 300$ μm and $w_{tot} = 150$ μm. As the GRF increases, the current flow departs from purely perpendicular to the finger although not nearly as much as for the FLPC. The maximum angle with respect to perpendicular at a GRF of 100 was approximately $16°$.

The directional change in the current flow seen Figure 36 occurred in the FLPC and not the OLPC because the effective sheet resistance for the former was much less. When multiple routes are available to current, it divides itself such that more current flows through paths of lower resistance which in this case was provided by the LCL for the FLPC and not in the OLPC. One would expect that for high enough GRFs, a similar directional change in current flow would occur in the OLPC.

Bearing in mind that current flow can be altered by shifting the relative resistance of the finger to the semiconductor layers, an increased finger resistivity given by a GRF of 100 was still used to explore how the finger length affected the

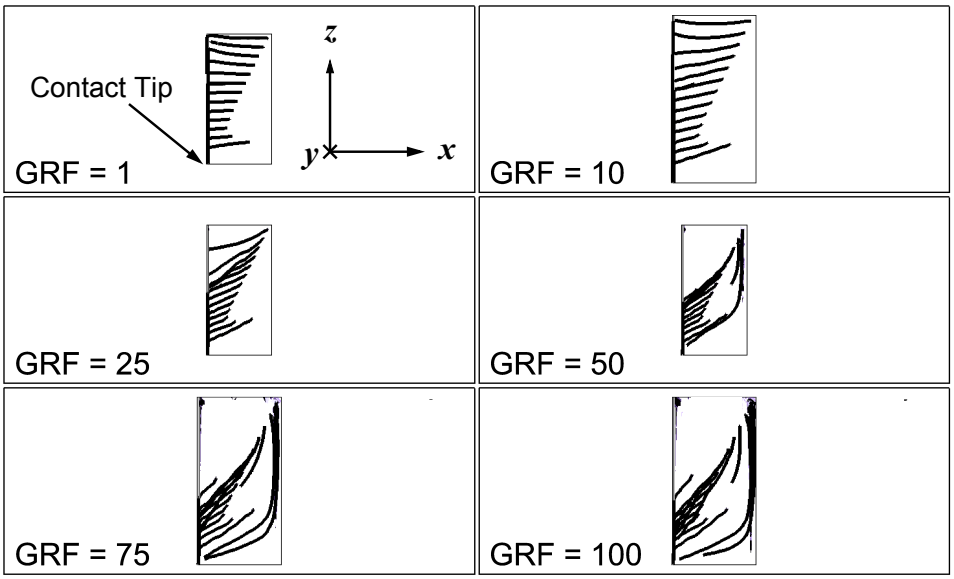

Figure 36. Current streamline plots for the FLPC with $z_{tot} = 300$ μm and $w_{tot} = 150$ μm. As the GRF increases, the current begins to flow parallel to the finger in the semiconductor layers. This represents a departure from the assumption of perpendicular current flow in the analytic model. Since less current flowed through the metal finger, the simulated finger losses were lower than the analytic model predicted.

losses and efficiency while saving the computation time needed to simulate very long devices before exploring the efficiency of cells with a GRF of 1.

5.3 3D Efficiency vs Finger Length

Fingers with a GRF of 100.

For large area devices on the order of $6 - 25$ cm^2, the simplest implementation would require finger lengths on the order of $2.5 - 5$ cm in length. As already mentioned in the last section this is not feasible with the present computational resources. Hence, a GRF of 100 with finger lengths of 100 to 500 μm (0.01 to 0.05 cm) was meant to reveal the same trends as simulating fingers of $0.1 - 0.5$ cm even though they are not exactly equivalent.

The fixed parameters for this set of simulations were the same as those in the previous section in which the GRF was varied with $w_{tot} = 150$ μm, $w_{front} = 3$ μm (effective width of 6 μm), and a finger height of 0.5 μm. Figure 37 shows the efficiencies of the LPCs as a function of z_{tot} with a GRF of 100.

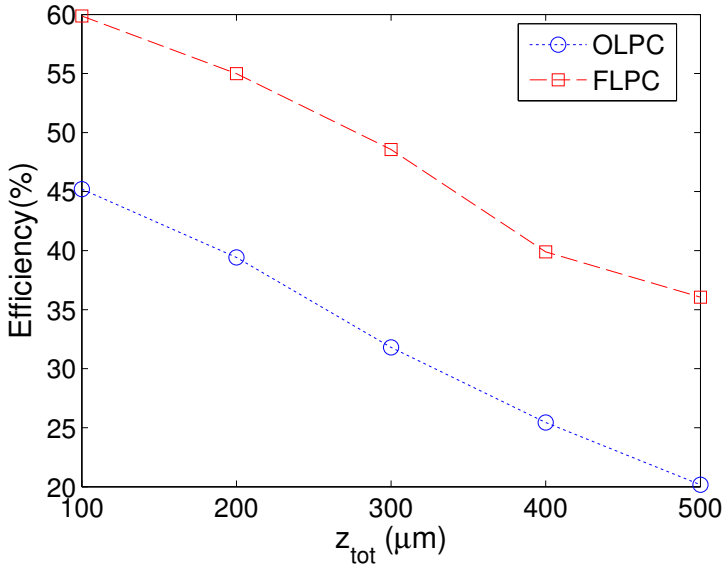

Figure 37. The efficiency of the LPCs with the resistivity of the gold fingers at 100 times their actual value. The finger dimensions are $H_f = 0.5$ μm and $w_{front} = 3$ μm (effective width of 6 μm).

Figure 37 shows that with the GRF set to 100, extending the device along the length of the finger resulted in an efficiency drop from the 2D simulation results. The efficiencies and FFs were compared to the 2D simulations as in the previous section and the results are summarized in Table 7.

Both results show that increasing the finger length significantly reduced the efficiency when the GRF was set to 100. The OLPC and FLPC show a similar drop in overall efficiency and FF with the FLPC having a smaller normalized drop in efficiency. The LCL likely mitigated some of the losses in the FLPC as the finger

Table 7. LPC performances with GRF=100 and z_{tot} reaching 500 μm

model	$\Delta\eta(\%)$	$\Delta\eta_{norm}(\%)$	$\Delta FF(\%)$
OLPC	26.74	57.00	31.55
FLPC	24.83	40.78	32.32

length was increased since it was shown in Figure 36 that for a GRF of 100, the current no longer flowed perpendicular to the finger.

Figures 38 and 39 show a comparison of the analytic finger loss with the simulated loss for the OLPC and the FLPC respectively.

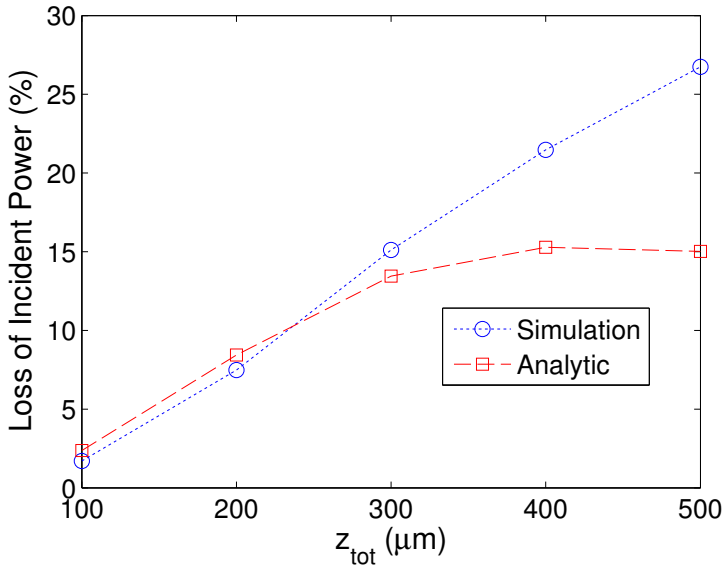

Figure 38. Comparison of the analytic and simulated finger losses for the OLPC with a GRF of 100. Comparison of the curves resulted in $R^2 = 0.563$. The divergence is likely due to a drop in output current as seen in the 2D models.

Figure 40 shows the FF of the LPCs as z_{tot} was increased for the cells with a GRF of 100.

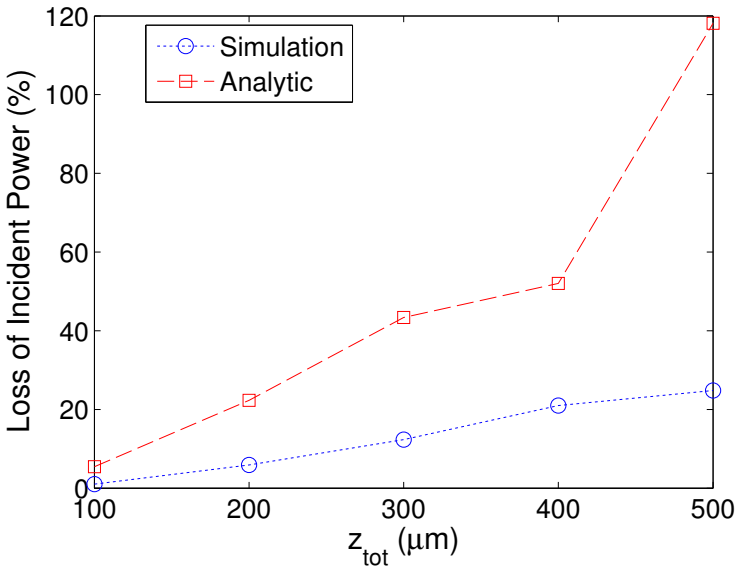

Figure 39. Comparison of the analytic and simulated finger losses for the FLPC with a GRF of 100. Comparison of the curves resulted in $R^2 = -26.41$ since the curves did not overlap. The significant difference between the curves is due to the current not flowing perpendicular to the finger at a GRF of 100 as shown in Figure 36.

As expected, the efficiency and FF both decrease as the finger length increases. Also, as we saw in the last section, the simulations indicate that the LCL layer does not follow the analytic model except for the shortest finger lengths indicating lateral conduction of correct parallel to the fingers is occurring in addition to perpendicular conduction.

Thin Fingers with a GRF of 1.

The grid metal fingers used in the concentrator solar cell optimization discussed in Section 3.2 were 0.5 μm thick and 3 μm wide which was relatively small compared to the typical widths of 5 μm with height/width aspect ratios near $0.6 - 1$ [13]. Nonetheless, in order to determine if the efficiency drops as a function of area reported by Algora, *etal.* in [3] were primarily the result of finger losses, the same finger cross-section was used with an unmodified gold resistivity value

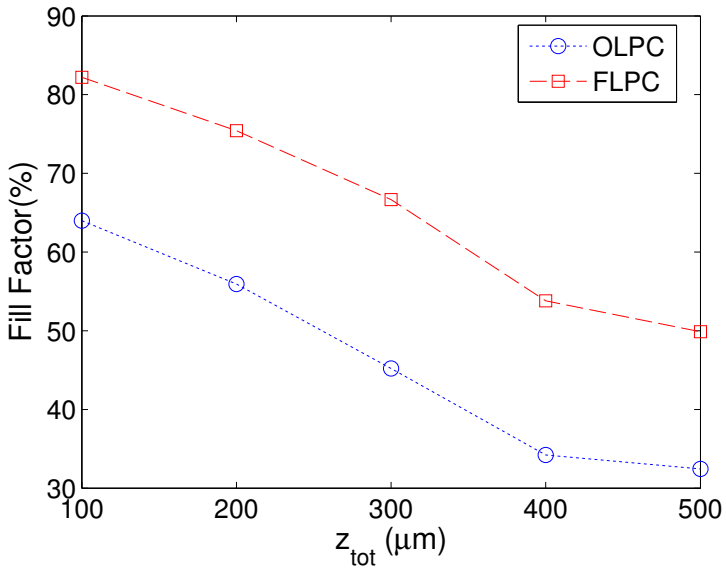

Figure 40. The fill factors of the LPCs with the resistivity of the gold fingers at 100 times their actual value. The finger dimensions are $H_f = 0.5$ μm and $w_{front} = 3$ μm (effective width of 6 μm).

(GRF = 1). Since the model is a unit cell with half of the finger width of an actual device, w_{front} was set to 1.5 μm with the thickness, H_f, set to 0.5 μm for both the OLPC and the FLPC to investigate whether the LCL would mitigate any of the series resistance contribution from extending the models along the finger length. Figure 41 shows that the FLPC showed a more severe drop in efficiency than the OLPC as the finger length was increased.

The figure shows efficiency dropped rapidly for both LPCs beyond a z_{tot} value of about 500 μm. Figure 42 shows the drop in FF for both LPCs as the z_{tot} was increased.

Table 8 summarizes how the LPCs performed at $z_{tot} = 2500$ μm compared to their 2D simulation counterparts. It shows that the FLPC suffered larger drops in efficiency and FF as z_{tot} increased to 2500 μm.

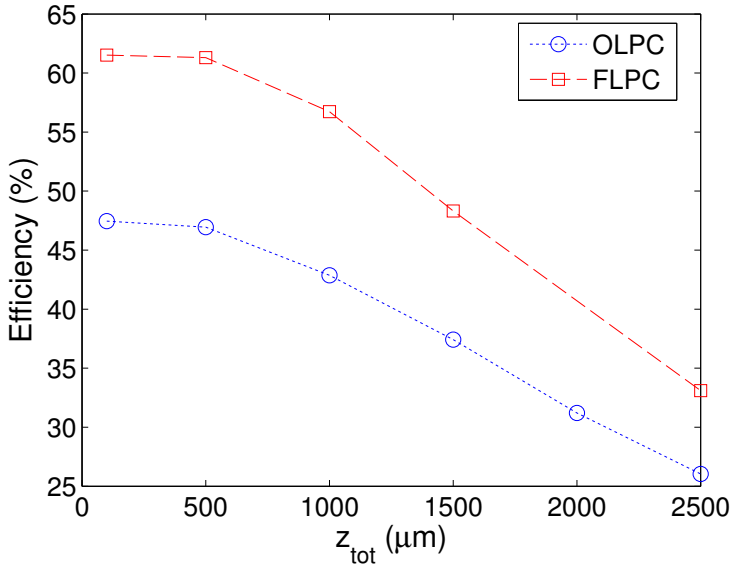

Figure 41. Simulation results from extending the models along the length of the finger when the finger dimensions matched those referenced in [3]. The efficiencies for the OLPC are compared with the FLPC to investigate the impact of the LCL and the results show that both models suffer significant loss when extended along the grid finger.

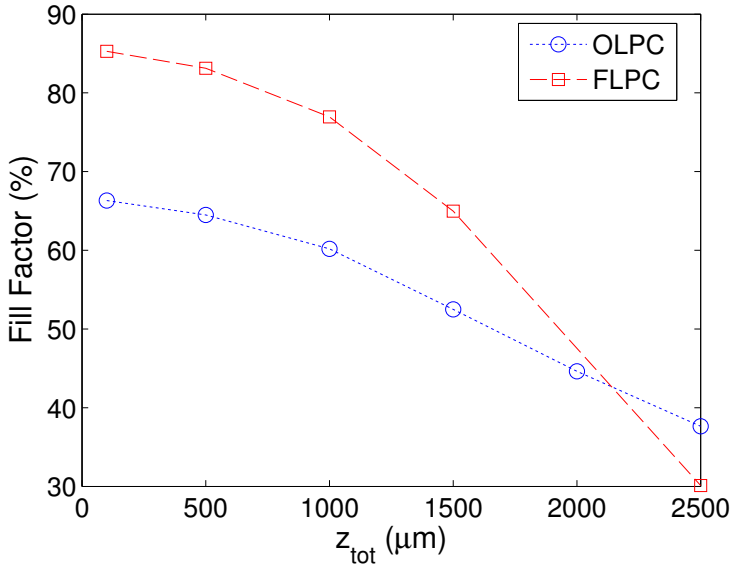

Figure 42. Simulation results from extending the models along the length of the finger when the finger dimensions matched those referenced in [3]. The fill factors for the OLPC are compared with the FLPC to investigate the impact of the LCL.

Table 8. LPC performances with z_{tot} reaching 2500 μm

model	$\Delta\eta(\%)$	$\Delta\eta_{norm}(\%)$	$\Delta FF(\%)$
OLPC	20.61	43.93	28.67
FLPC	27.45	45.09	55.18

The analytically predicted finger losses were compared with the simulated losses and are shown in Figure 43 and 44 for the OLPC and FLPC respectively. Both figures show good agreement between the analytic and simulated losses up to $z_{tot} = 1500$ μm after which the analytic model underestimated the losses found in the simulation. This is due to the drop in current that occurred as the finger length increased. As discussed in Section 5.1, a drop in the output current lowers analytic model which has a squared dependence on current but decreases the efficiency (increasing the simulated losses). This manifests itself in the divergence between the simulated losses and analytic losses in Figures 43 and 44.

Even though the simulated and analytic losses diverge at large value of z_{tot}, the important result is that the efficiencies were not maintained as the finger length increased using finger dimensions that matched those used in investigating the efficiency of a GaAs CPV in [3]. To compare the results of increasing the finger length with the results presented in Figure 1, the results in Figure 42 were interpolated and used as described in Section 4.7 to predict the efficiencies of the OLPC and FLPC as a function of area for both the parallel and inverse square metal grid designs. Figure 45 shows the resulting efficiency estimates.

Figure 45 is meant to show how the efficiency can drop with area for both grid configuration as a result of lengthening the grid fingers rather than increasing the finger spacing. Actual device efficiencies using these grids are expected to differ from the estimates due to current flowing directly to the busbar which might

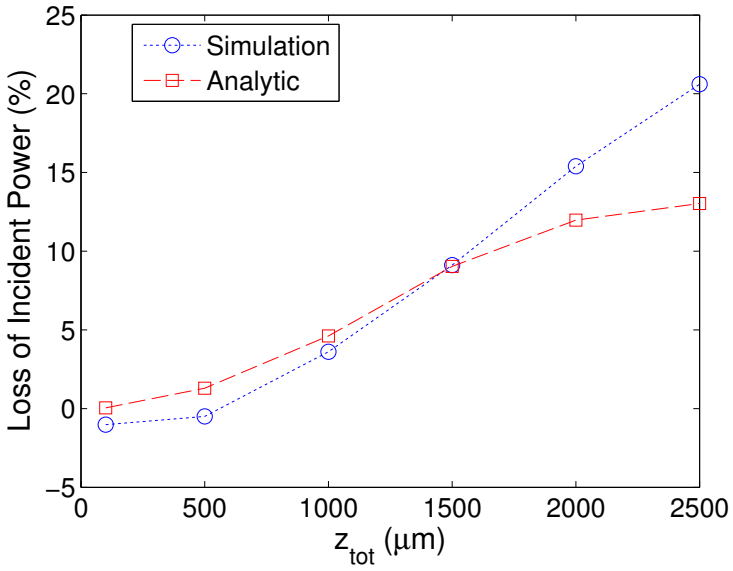

Figure 43. Comparison of the analytic and simulated finger losses for the OLPC with $w_{front} = 1.5$ μm (effective width of 3 μm) and finger height of 0.5 μm. Comparison of the curves resulted in $R^2 = 0.806$. The divergence is likely due to a reduction in output current at high value of z_{tot} that reduces the efficiency of the device but is not part of the resistive loss.

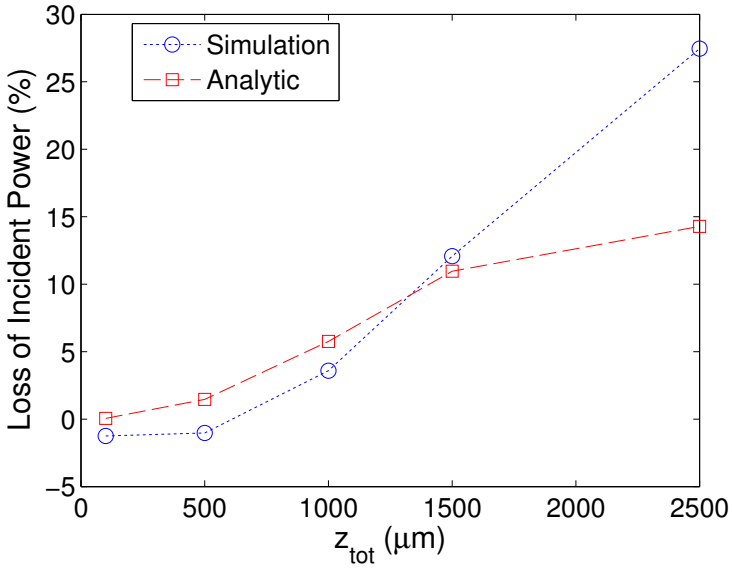

Figure 44. Comparison of the analytic and simulated finger losses for the FLPC with $w_{front} = 1.5$ μm (effective width of 3 μm) and finger height of 0.5 μm. Comparison of the curves resulted in $R^2 = 0.678$. The divergence is likely due to a reduction in output current at high value of z_{tot} that reduces the efficiency of the device but is not part of the resistive loss.

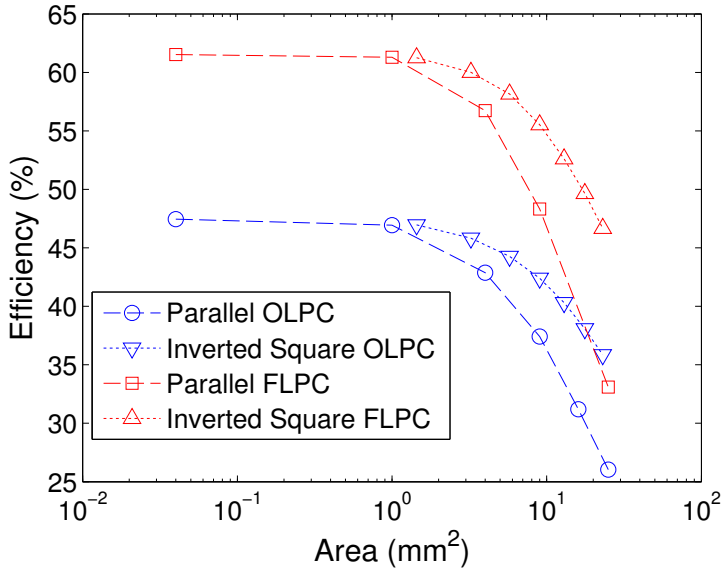

Figure 45. The estimated efficiencies as a function of area for the parallel and inverted square grids for the OLPC and FLPC. The efficiencies were predicted by interpolating the simulation results for different unit cell sizes.

increase the efficiency. The increase in efficiency due to direct current flow to the busbar would likely be counteracted by the increase in temperature in the device along with the presence of contact resistance which were not accounted for in the simulation. Since both devices showed a significant drop in efficiency, it is apparent that the LCL did not mitigate the increased resistance introduced by lengthening the metal grid fingers and another technique is necessary to achieve a high efficiency, large area LPC.

Thick fingers with a GRF of 1.

In order to see if increasing the finger cross section could help maintain the efficiency of the devices for long finger lengths, the finger on the OLPC design was increased to a thickness of 5 μm with an effective width of 10 μm ($w_{front} = 5$ μm) and the model was again simulated having various finger lengths. Figure 46 shows a

comparison of the finger cross sections and Figure 47 shows a comparison of efficiencies of the OLPC models having thick and thin fingers.

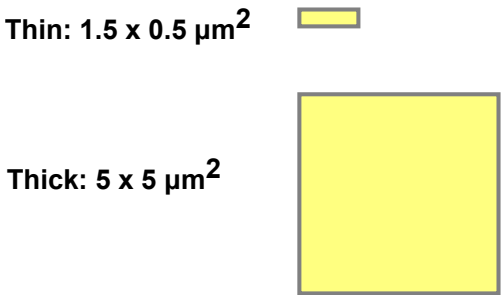

Figure 46. Comparison of the finger cross-sections used on the unit cells shown in relative scale. These represent half the width of the fingers of actual devices since they are used on the model unit cell.

The efficiency of the device with thin fingers dropped significantly down to 26% for a finger length of only 2500 μm whereas the efficiency of the model with thick fingers only dropped to 44.89% for a finger length of 5000 μm.

Figure 48 shows a comparison of the analytic model to the simulated losses for the OLPC with thick fingers. This figure shows that both the analytic and simulated losses are less than 0.34 W/cm^2. As previously mentioned, the negative losses indicate that the 3D simulation performed better than its 2D counterpart even when shadowing losses were accounted for. The fill factors of the OLPC models with different finger thicknesses are shown in Figure 49.

Figures 47 and 49 show that increasing the finger thickness can significantly reduce the contribution of the grid metal fingers to the total series resistance losses. While simulations did not converge for devices beyond 5000 μm, the efficiency drop at this length was minimal, indicating longer fingers may be possible in actual devices without significant finger losses if the fingers are sufficiently thick.

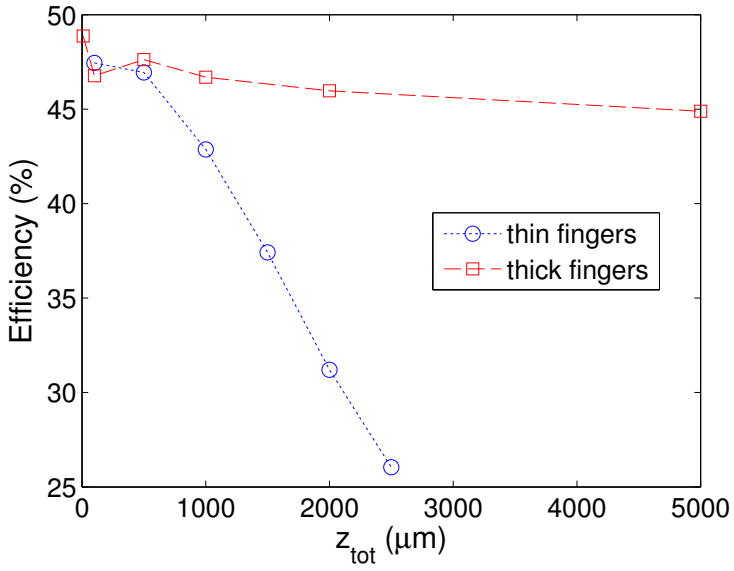

Figure 47. Simulation results of the original GaAs LPC comparing the thick ($5\ \mu\text{m} \times 5\ \mu\text{m}$) **metal finger cross-section with the thin** ($1.5\ \mu\text{m} \times 0.5\ \mu\text{m}$) **as the length of the fingers increased. The efficiency of the device with thin fingers drops significantly down to** 26% **for a finger length of** $2500\ \mu\text{m}$ **whereas the efficiency of the model with thick fingers only drops to** 44.89% **for a finger length of** $5000\ \mu\text{m}$**.**

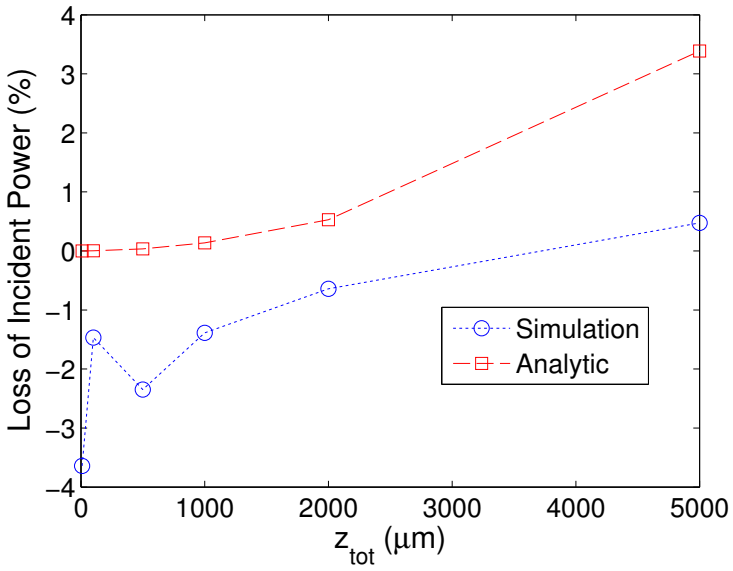

Figure 48. Comparison of the analytic and simulated finger losses for the OLPC with $w_{front} = 5$ μm (effective width of 10 μm) and finger height of 5 μm. Comparison of the curves resulted in $R^2 = -2.34$ since the curves did not overlap. The losses in both cases are much smaller than an of the other simulation sets which magnifies the difference. As previously mentioned, the negative values of loss indicate that the 3D model outperformed its 2D counterpart which helps reveal possible magnitude of uncertainty in all of the simulation results.

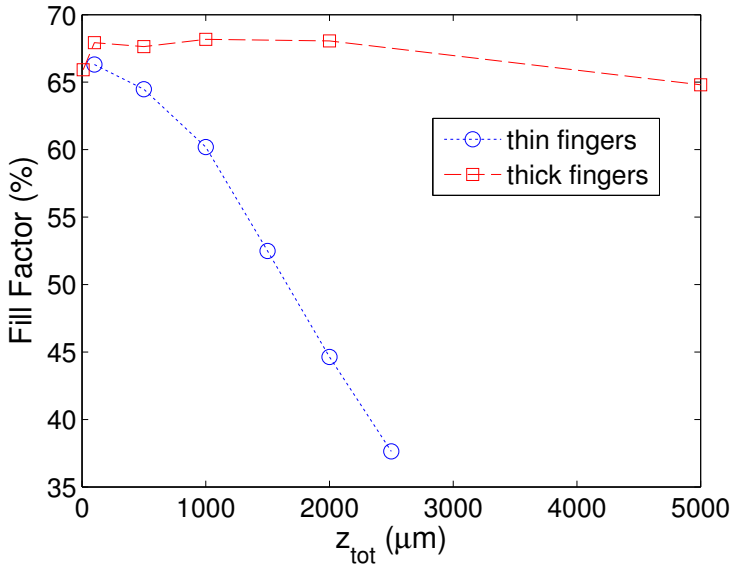

Figure 49. The fill factor of the original LPC with two different metal finger dimensions. The cell with the thick ($5\ \mu\text{m} \times 5\ \mu\text{m}$) metal finger cross-section maintains a high fill factor, dropping from about 68% to 64% as the finger length extended to $5000\ \mu\text{m}$. The cell with the thin ($1.5\ \mu\text{m} \times 0.5\ \mu\text{m}$) metal finger on the other hand showed a drop in fill factor from 66.31% down to 37.64% when extending the finger to only $2500\ \mu\text{m}$.

VI. Conclusions

6.1 Findings

The results and the analysis in the previous section lead to several recommendations about the structural attributes of a Laser Power Converter that might allow it to maintain efficiency while its area is increased toward AFRL's design goal of 6 cm^2 or more. First of all, it is apparent that AFRL's metallization scheme needs to be improved so the contact resistance is not a problem since most of the contact resistivity values on both the n and p type InP wafers were at or above $10^{-3}\ \Omega - cm^2$. Next, the comparison of the Fraunhofer Institute based design to the original GaAs LPC revealed the importance of the highly doped Lateral Conduction Layer in mitigating the series resistance losses in the window/emitter layer for higher finger spacings. The 2D OLPC simulations results showed $\Delta\eta$ of 39.43% and $\Delta\eta_{norm}$ of 66.34% when w_{tot} was increased to 370 μm whereas the 2D FLPC showed a smaller drop in efficiency and FF given by a $\Delta\eta$ of 14.38% and a $\Delta\eta_{norm}$ of 23.29% when w_{tot} was increased to 500 μm which was even further than the OLPC was extended.

In addition to the LCL, the results comparing the performance of the devices with differing finger cross-sections showed that a thicker finger can help maintain efficiency as the device is extending along the length of the finger. The model with thicker fingers showed a $\Delta\eta$ of only 0.47% when extended out to 5000 μm while the model with thin fingers showed a $\Delta\eta$ of 20.61% when extended to 2500 μm. The combination of thick fingers with an LCL will be key in creating a large area LPC operating at high light intensities.

The inversion of the cell may make it possible to combine the benefits of thick fingers and an LCL. In the inverted design, the top layer of the device is the

substrate. By ensuring the substrate is highly doped such that it is very conductive (doping on the order of 10^{19} cm^{-3}) it may act as the LCL. However, there may be limits to the doping level that can be used. The experimental results from the Fraunhofer Institute indicate that high doping levels in the LCL layers can be a problem. Direct bandgap related absorption of the 1550 nm source by the InP substrate (bandgap of 919 nm) is not a problem but free carrier absorption and other doping related absorption effects need to be considered. There is not much information available in the literature on this subject so it may be necessary to measure the optical absorption to determine if it is a major concern or not.

By having a thick substrate on top, it may be possible to create high aspect ratio (up to 5 μm $\times$ 20 μm) trenches in which the grid metal can be deposited. This will allow for cross-sectional areas of up to 100 μm^2 which is even larger than the 50 μm^2 "thick" fingers modeled on the OLPC. This has the additional benefit of leaving the top surface smooth, making the application of anti-reflection coatings easier.

6.2 Future Work

The simulation results showed the general trends to be expected as the finger spacing and finger lengths were increased in the models. The next step will be to model the AFRL baseline design and optimize the layer thicknesses, doping levels, and grid design. If an LCL is included in future designs, the models should investigate the effects of free carrier absorption which may become a problem at high doping levels. Additionally, the temperature effects could be included in the simulation, including a heat sink on the bottom of the device to investigate how cell inversion allows the device to be cooled more efficiently.

On the fabrication side, as mentioned in the discussion of the TLM results in Section 4.1, the metallization process will have to be further explored to achieve

consistent contact resistivities below $10^{-4}\ \Omega - \mathrm{cm}^2$. Additionally, future work could include trenching InP wafers and depositing metal in the trenches. These samples would need to maintain low contact resistance and could be explored for their reflection, transmission, and absorption of 1550 nm light to quantify the benefits of trenching the grid metal. After fabricating baseline LPCs, the next step will be to test them under actual laser illumination.

Previous research has demonstrated a variety of methods for determining the performance of PV cells using the characteristic current/voltage (IV) curve of the device [25]. Additional testing methods have been developed to specifically determine the resistance features of the device [26][12]. In order to adapt and apply the techniques for testing PV cells, a testing system will need to be designed specifically to evaluate the performance of the intermediate and end result LPC designs. Most commercial PV cell testing equipment is designed for testing cells that convert broad spectrum solar radiation that operate at lower power levels than those required for laser power conversion. The test system for prototype LPCs will need to include a 1550 nm laser, a method of expanding the beam to simulate the effects of propagation over large distances, a voltage source to bias the cell, and a multimeter for measuring the IV characteristics of the cell to determine the power output and efficiency

The test results should be compared to the simulation results where possible to validate the characterization and proposed mitigation of resistive losses in a large area Laser Power Converter.

References

1. R. Mason, "Feasibility of laser power transmission to a high-altitude unmanned aerial vehicle," RAND Corporation, Tech. Rep., 2011. [Online]. Available: www.rand.org/content/dam/rand/pubs/technical_reports/2011/RAND_TR898.pdf

2. G. Martinelli and M. Stefancich, "Typical structure of a cell-to-sink interconnect," in *Concentrator Solar Cells*, W. T. Rhodes, Ed. Springer, 2007, ch. Solar Cell, pp. 133–149.

3. C. Algora and V. Diaz, "Influence of series resistance on guidelines for manufacture of concentratror p-on-n GaAs solar cells," *Progress in Photovoltaics*, vol. 8, no. 2, pp. 211–225, 2000.

4. B. Beaumont, J. Guillaume, A. Vilela, A. Saletes, and C. Verie, "High efficiency conversion of laser energy and its application to optical power transmission," in *Photovoltaic Specialists Conference*, no. i, Las Vegas, NV, 1991, pp. 1503–1507.

5. R. Muller and T. Kamins, *Device Electronics for Integrated Circuits*, 3rd ed., V. Vargas, Ed. New York: Wiley, 2003.

6. E. L. Dereniak and G. D. Boreman, *Infrared Detectors and Systems*, J. Goodman, Ed. Agawam, MA: Wiley-Interscience, 1996.

7. S. Wojtczuk, S. Vernon, and E. Gagnon, "InGaAs concentrator cells for laser power converters and tandem cells," in *Proceedings of the 12th Space Photovoltaic Research and Technology Conference*, 1993, pp. 119–128.

8. R. K. Jain, "Suitability of InP window layers for InGaAs solar cells," in *Proceedings of 3rd World Conference on Photovoltaic Energy Conversion 2003*, vol. 1, Osaka, Japan, 2003, pp. 75–78.

9. A. W. Bett, F. Dimroth, R. Lockenhoff, E. Oliva, J. Schubert, and D. Freiburg, "III-V Solar cells under monochromatic illumination," in *Photovoltaic Specialists Conference*, San Diego, CA, 2008, pp. 1–5.

10. D. E. Raible, "Free space optical communications with high intensity laser power beaming," Ph.D. dissertation, Cleveland State University, 2011.

11. P. J. Gress and S. Varlamov, "Quantification of power losses of the interdigitated metallization of crystalline Silicon thin-film solar cells on glass," *International Journal of Photoenergy*, vol. 2012, no. [Special Section], pp. 1–6, 2012.

12. D. Pysch, A. Mette, and S. Glunz, "A review and comparison of different methods to determine the series resistance of solar cells," *Solar Energy Materials and Solar Cells*, vol. 91, no. 18, pp. 1698–1706, Nov. 2007.

13. A. Luque and S. Hegedus, Eds., *Handbook of photovoltaic science and engineering*, 2nd ed. Chichester, West Sussex, UK: Wiley, 2011.

14. B. E. A. Saleh and M. C. Teich, *Fundamentals of Photonics*, 2nd ed., B. E. A. Saleh, Ed. Hoboken, NJ: John Wiley & Sons, Inc., 2007.

15. S. Wenham, C. Honsberg, and M. Green, "Buried contact silicon solar cells," *Solar Energy Materials and Solar Cells*, vol. 34, no. 1-4, pp. 101–110, Sep. 1994.

16. C. Algora and V. Diaz, "Guidance for reducing photovoltaic cost using very high concentrator GaAs solar cells," in *14th European Photovoltaic Solar Energy Conference*, Barcelona, Spain, 1997, pp. 1724–1727.

17. ——, "Design and optimization of very high power density monochromatic GaAs photovoltaic cells," *IEEE Transactions on Electron Devices*, vol. 45, no. 9, pp. 2047–2054, 1998.

18. S. Daliento and L. Lancellotti, "3D Analysis of the performances degradation caused by series resistance in concentrator solar cells," *Solar Energy*, vol. 84, no. 1, pp. 44–50, Jan. 2010.

19. T. Gessert, X. Li, and T. Coutts, "Practical guidelines for grid metallization in photovoltaic solar cell research," *Solar Cells*, vol. 30, no. 1-4, pp. 459–472, 1991.

20. Synopsys, "Simulation of 2D single-junction GaAs solar cell," 2013. [Online]. Available: https://solvnet.synopsys.com/retrieve/039247.html

21. ——, "Mesh Generation Tools User Guide," 2013. [Online]. Available: https://solvnet.synopsys.com/dow_retrieve/latest/ni/tcad.html#Tcad

22. ——, "Sentaurus Device User Guide," 2013. [Online]. Available: https://solvnet.synopsys.com/dow_retrieve/latest/ni/tcad.html#Tcad

23. Brigham Young University. Dept. of ECE, "Anti-Reflection Thickness Calculator," 2013. [Online]. Available: http://www.photonics.byu.edu/ARcoatings.phtml

24. J. Li, D. Ding, S. H. Lim, and Y. Zhang, "Contact optimization for concentrator solar cells," in *Photovoltaic Specialists Conference*, no. 4, Honolulu, HI, 2010, pp. 2074–2078.

25. A. Hovinen, "Fitting of the solar cell IV-curve to the two diode model," *Physica Scripta*, vol. T54, pp. 175–177, 1994.

26. L. Ma, L. Xu, K. Zhang, W. Wu, and Z. Ma, "The measurement of series and shunt resistances of the silicon solar cell based on LabVIEW," in *2011 International Conference on Electrical and Control Engineering*. Yichang, China: IEEE, Sep. 2011, pp. 2711–2714.

Vita

Eli Garduño was born in Santa Fe, NM where he graduated from Santa Fe High School in 2008 as the class Valedictorian. He attended the United States Air Force Academy in Colorado Springs, CO earning a Bachelor of Science Degree in Physics with a minor in Chinese. He graduated as a Distinguished Graduate in the class of 2012, earning a commission as a Second Lieutenant and was selected to attend the Graduate School of Engineering and Management at the Air Force Institute of Technology at Wright-Patterson AFB, OH, to obtain a Master's Degree in Applied Physics. Following graduation, he will be assigned to Kirtland AFB, NM in the Space Vehicles Directorate.

REPORT DOCUMENTATION PAGE

Form Approved
OMB No. 0704–0188

1. REPORT DATE *(DD–MM–YYYY)*	2. REPORT TYPE	3. DATES COVERED *(From — To)*
27–03–2014	Master's Thesis	Oct 2012 - Mar 2014

4. TITLE AND SUBTITLE

Characterization and Mitigation of Resistive Losses in a Large Area Laser Power Converter

5a. CONTRACT NUMBER

5b. GRANT NUMBER

5c. PROGRAM ELEMENT NUMBER

6. AUTHOR(S)

Garduño, Eli A., 2LT, USAF

5d. PROJECT NUMBER

N/A

5e. TASK NUMBER

5f. WORK UNIT NUMBER

30011213

7. PERFORMING ORGANIZATION NAME(S) AND ADDRESS(ES)

Air Force Institute of Technology
Graduate School of Engineering and Management (AFIT/EN)
2950 Hobson Way
WPAFB OH 45433-7765

8. PERFORMING ORGANIZATION REPORT NUMBER

AFIT-ENP-14-M-09

9. SPONSORING / MONITORING AGENCY NAME(S) AND ADDRESS(ES)

Gernot Pomrenke
Air Force Office of Scientific Research
875 North Randolph Street
Arlington, VA, 22203-1768
426-8426, gernot.pomrenke@afosr.af.mil

10. SPONSOR/MONITOR'S ACRONYM(S)

AFOSR

11. SPONSOR/MONITOR'S REPORT NUMBER(S)

12. DISTRIBUTION / AVAILABILITY STATEMENT

DISTRIBUTION STATEMENT A: APPROVED FOR PUBLIC RELEASE; DISTRIBUTION UNLIMITED.

13. SUPPLEMENTARY NOTES

14. ABSTRACT

GaAs Laser Power Converters (LPC) were simulated in 2D and 3D under 10 W/cm^2 illumination of 810 nm light using Synopsys Sentaurus software revealing significant dependence of efficiency on grid metal finger spacings, S, and finger dimensions. Efficiency results were comparable to an experimental efficiency of 53.4% cited in the literature for an LPC under 43 W/cm^2 of 810 nm laser light. 2D devices were simulated with S of $20 - 1000$ μm revealing an efficiency drop, $\Delta\eta$, with increasing spacings. The efficiency drop was reduced from $\Delta\eta$ of 39.43% at $S = 740$ μm to $\Delta\eta$ of 14.38% at $S = 1000$ μm when modifying the window layer to include a highly doped lateral conduction layer (LCL). In the 3D simulations, resistive losses in the grid metal fingers were reduced by thickening the grid metal from 3 μm $\times$ 0.5 μm with an efficiency of 26% at an effective length of 0.5 cm up to 10 μm $\times$ 5 μm, achieving an efficiency of 44.89% at an effective finger length of 1 cm. An LCL and thicker fingers are shown to be critical for designing large area LPCs to convert laser light to electrical power for devices such as small RPAs and tactical sensors.

15. SUBJECT TERMS

Laser Power Converter, Solar Cell, Photovoltaic, Grid Resistance

16. SECURITY CLASSIFICATION OF:			17. LIMITATION OF ABSTRACT	18. NUMBER OF PAGES	19a. NAME OF RESPONSIBLE PERSON
a. REPORT	b. ABSTRACT	c. THIS PAGE			Maj Timothy W. Zens
U	U	U	UU	119	19b. TELEPHONE NUMBER *(include area code)* (937)255-3636 x4469; Timothy.Zens@afit.edu